

Novel methods for detection of small RNAs and
photo-dependent intercellular delivery of biomolecules

低分子 RNA の蛍光検出と生体分子の
光依存的細胞内導入のための新手法開発

March, 2020

Yuichi Miyoshi

Graduate school of
Natural Science and Technology
(Doctor's course)

OKAYAMA UNIVERSITY

Contents

General Introduction	1
References	3
Chapter 1	
Detection of mature tRNA by using in-stem molecular beacon	
Abstract	7
Introduction	9
Materials and Methods	12
Results	23
Discussion	37
References	41
Chapter 2	
Endosomal escape of peptide-photosensitizer conjugates is affected by amino acid near the photosensitizer	
Abstract	49
Introduction	51
Materials and Methods	55

Results	61
Discussion	74
References	78
List of publications	84
Acknowledgment	85

General Introduction

Photochemical approaches, such as fluorescence bioimaging¹ and photo-control of cellular functions^{2,3}, have been widely used in biology.

Fluorescence imaging of RNAs (Chapter 1)

To date, various types of RNAs have been studied to elucidate their function and localization⁴⁻⁶. To know cellular functions of RNAs, methods for imaging cellular RNA have been developed⁷. In addition, methods for detection and fluorescence bioimaging of RNA biomarkers for various diseases are essential⁸⁻¹⁰. However, most conventional methods are designed to target long RNA which have flexible single strand region. Therefore, conventional methods are difficult to use for imaging highly structured small RNAs. In this study, we investigated the design of fluorescent probes for detecting highly structured small RNAs.

Photo-control of cellular function using photosensitizers (Chapter 2)

Photosensitizers (PS) are used for treating cancer with minimal invasion, called photodynamic therapy (PDT)^{11,12}. In PDT mechanism, photogenerated reactive oxygen species (ROS) from PS damages cell tissue and be able to cause cell death. PS is also used for photoinducing cytosolic internalization of macromolecules such as nucleic acids and proteins, called photochemical internalization (PCI)¹³⁻¹⁵. Mechanism of PCI is

similar to PDT. PCI can control release of macromolecules into cytoplasm spatiotemporally. PCI-based phototherapy has been demonstrated by delivering therapeutic molecules¹⁶⁻¹⁸. Therefore, methods to induce effective PCI has been required.

In this work, we considered optimal design of peptide-photosensitizer conjugates, which can be efficiently delivered into cytosol by the PCI mechanism.

References

- (1) Specht EA, Braselmann E, Palmer AE. (2017) A critical and comparative review of fluorescent tools for live-cell imaging. *Annu Rev Physiol.* 79, 93–117.
- (2) Selbo PK, Weyergang A, Høgset A, Norum OJ, Berstad MB, Vikdal M, Berg K. (2010) Photochemical internalization provides time- and space-controlled endolysosomal escape of therapeutic molecules. *J Control Release.* 148, 2–12.
- (3) Kwiatkowski S, Knap B, Przystupski D, Saczko J, Kędzierska E, Knap-Czop K, Kotlińska J, et al. (2018) Photodynamic therapy-mechanisms, photosensitizers and combinations. *Biomed Pharmacother.* 106, 1098–1107.
- (4) Hsiao KY, Sun HS, Tsai SJ. (2017) Circular RNA - new member of noncoding RNA with novel functions. *Exp Biol Med (Maywood).* 242, 1136-1141.
- (5) Neriec N, Pericipalle P. (2018) Sorting mRNA molecules for cytoplasmic transport and localization. *Front Genet.* 9, 510.
- (6) Chatterjee K, Nostramo RT, Wan Y, Hopper AK. (2018) tRNA dynamics between the nucleus, cytoplasm and mitochondrial surface: location, location, location. *Biochim Biophys Acta Gene Regul Mech.* 1861, 373-386.
- (7) Xia Y, Zhang R, Wang Z, Tian J, Chen X. (2017) Recent advances in high-performance fluorescent and bioluminescent RNA imaging probes. *Chem Soc Rev.* 46, 2814-28434.
- (8) Peng Y, Croce CM. (2016) The Role of MicroRNAs in Human Cancer. *Signal*

Transduct Target Ther. 1, 15004.

- (9) Sun Z, Shi K, Yang S, Liu J, Zhou J, Zhou Q, Wang G, et al. (2018) Effect of exosomal miRNA on cancer biology and clinical applications. *Mol Cancer.* 17, 147.
- (10) Sun C, Fu Z, Wang S, Li J, Li Y, Zhang Y, Yang F, et al. (2018) Roles of tRNA-derived fragments in human cancers. *Cancer Lett.* 414, 16-25.
- (11) Juarranz A, Jaén P, Sanz-Rodríguez F, Cuevas J, González S, et al. (2008) Photodynamic therapy of cancer. Basic principles and applications. *Clin Transl Oncol.* 10, 148-154.
- (12) Hwang HS, Shin H, Han J, Na K. (2018) Combination of photodynamic therapy (PDT) and anti-tumor immunity in cancer therapy. *J Pharm Investig.* 48, 143-151.
- (13) Oliveria S, Fretz MM, Høgset A, Storm G, Schiffelers RM. (2007) Photochemical internalization enhances silencing of epidermal growth factor receptor through improved endosomal escape of siRNA. *Biochim Biophys Acta.* 1768, 1211-1217.
- (14) Fretz MM, Høgset A, Koning GA, Jiskoot W, Storm G. (2007) Cytosolic delivery of liposomally targeted proteins induced by photochemical internalization. *Pharm Res.* 24, 2040-2047.
- (15) Berg K, Selbo PK, Prasmickaite L, Tjelle TE, Sandvig K, Moan J, Gaudernack

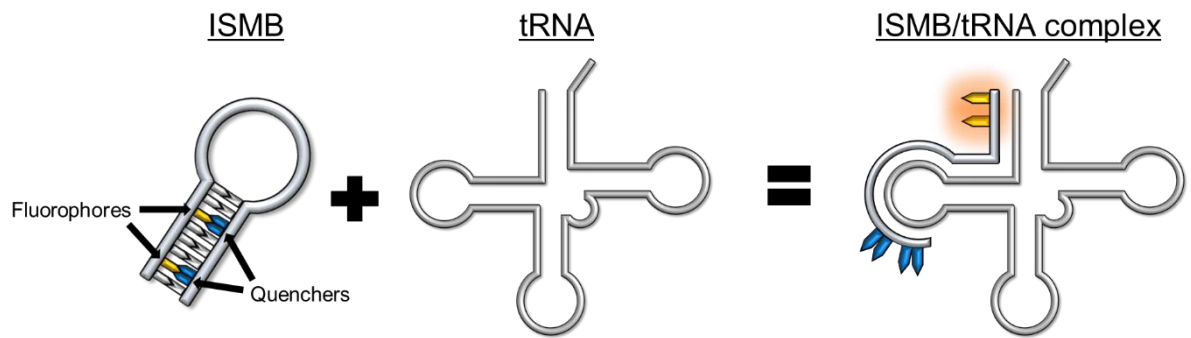
- G, et al. (1999) Photochemical internalization: a novel technology for delivery of macromolecules into cytosol. *Cancer Res.* 59, 1180–1183.
- (16) Šošić L, Selbo PK, Kotkowska ZK, Kündig TM, Høgset A, Johansen P. (2020) Photochemical internalization: light paves way for new cancer chemotherapies and vaccines. *Cancers (Basel)*. 12, 165.
- (17) Shin D, Chritie C, Ju D, Nair RK, Molina S, Berg K, Krasieva TB, et al. (2018) Photochemical internalization enhanced macrophage delivered chemotherapy. *Photodiagnosis Photodyn Ther.* 21, 156-162.
- (18) Berg K, Folini M, Prasmickaite L, Selbo PK, Bonsted A, Engesaeter BØ, Zaffaroni N, et al. (2007) Photochemical internalization: a new tool for drug delivery. *Curr Pharm Biotechnol.* 8, 362-372.

Chapter 1

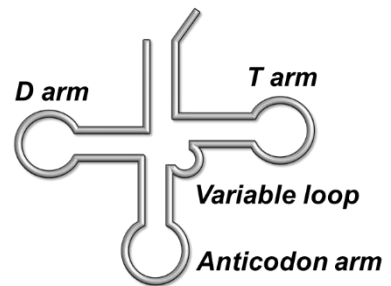
Detection of mature tRNA by using in-stem molecular beacon

Abstract

Cellular functions are regulated by the up- and down-regulation and localization of RNA molecules. Therefore, many RNA detection methods have been developed to analyze RNA levels and localization. Molecular beacon (MB) is one of the major methods for quantitative RNA detection and analysis of RNA localization. Most oligonucleotide-based probes, including MB, are designed to target a long flexible region on the target RNA molecule, e.g., a single-stranded region. Recently, analyses of tRNA localization and levels became important, as it has been shown that environmental stresses and chemical reagents induce nuclear accumulation of tRNA and tRNA degradation in mammalian cells. However, tRNA is highly structured and does not harbor any long flexible regions. Hence, only a few methods are currently available for detecting tRNA. In the present study, we attempted to detect elongator tRNA^{Met} (eMet) and initiator tRNA^{Met} (iMet) by using an in-stem molecular beacon (ISMB), characterized by more effective quenching and significantly higher sensitivity than those of conventional MB. We found that ISMB1 targeted a 5'-region that includes the D arm of tRNA and that it detected eMet and iMet transcripts as well as mature eMet with high sensitivity. Moreover, the analysis revealed that the formation of the ISMB/tRNA transcript complex required more time than the formation of an ISMB/unstructured short RNA complex. These results suggest that ISMB-based tRNA detection can be a useful tool for various biological and medical studies.



Which regions are effective to detect tRNA ?



Graphical abstract of this study

Introduction

Up- and down-regulation of expression and localization of RNA molecules are associated with the regulation of cellular functions^{1,2}. For instance, the up- and down-regulation of mRNA and miRNA levels regulates cell differentiation³. The localization of mRNA contributes to the regulation of local translation at the synapse^{4,5}. Therefore, RNA detection methods, such as northern blotting, reverse-transcription polymerase chain reaction, microarray analysis, fluorescent probes, and fluorescence in situ hybridization (FISH), have been developed to analyze RNA levels and localization⁶⁻⁹.

Methods using fluorescent probes, such as molecular beacons (MBs), have been developed as one of the major RNA detection approaches¹⁰. MB, which was first reported by Tyagi et al.¹¹, is a hairpin oligonucleotide with a fluorophore and a quencher in close proximity. Fluorescence of the fluorophore is quenched in the absence of target RNA. In the presence of target RNA, MB hybridizes with it by opening a stem region, and thereby the fluorescence intensity increases. MB can be used for quantitative RNA detection both in vitro and in vivo, and for evaluation of RNA localization^{9,12,13}.

It has been recently shown that initiator tRNA^{Met} (iMet) is degraded by exonucleases Xrn1 and Xrn2, to suppress translation in heat-stressed HeLa cells^{14,15}. In addition, it has been shown that iMet and elongator tRNA^{Met} (eMet) accumulate in the nucleus in heat-stressed HeLa cells, and then localize in the nuclear stress bodies¹⁶. Further, tRNAs accumulate in the nucleus of puromycin-treated Chinese hamster ovary cells¹⁷. In these

studies, northern blotting, FISH, and fluorescently labeled tRNA were mainly employed for quantitative tRNA detection and observation of tRNA localization, since only a few methods are currently available for the detection of tRNA molecules in mammalian cells.

Most oligonucleotide-based probes, including MB, are designed to target a long flexible region on the target RNA molecule, such as a single-stranded region ⁹. On the other hand, tRNA is highly structured and does not harbor any long flexible regions (Fig. 1-1A). Therefore, detecting tRNA molecules by using oligonucleotide-based probes, such as MB, might be difficult. To overcome this problem, we have recently attempted to detect tRNA transcripts by using conventional MBs targeting the various regions of a tRNA molecule ¹⁸. We have previously shown that conventional MB that targets the D arm of a tRNA^{Lys3} transcript can detect the tRNA^{Lys3} transcript with higher sensitivity than MBs targeted to the anticodon arm and the T arm. However, detection sensitivity of a tRNA transcript by using conventional MB was low. Furthermore, it remains unknown whether MB can detect mature tRNA molecules that contain multiple modified nucleotides because modified nucleotides might affect the hybridization with MB. Accordingly, we proposed to employ an in-stem molecular beacon (ISMB) that targets another region of tRNA (Fig. 1-1A). ISMB, in which two fluorophores and four quenchers are incorporated into the stem region as pseudo-base pairs, exhibit effective quenching and significantly higher sensitivity than conventional MB bearing a single fluorophore at one end and a single quencher at the other end of the stem region ¹⁹⁻²². The strong quenching of ISMB

is considered to be due to the pseudo-base pairing of fluorophore(s) and quencher(s). In the current study, we designed eight ISMB molecules for detecting iMet, eMet transcript, and mature eMet. We identified the best target region that enabled ISMB to detect tRNA with high sensitivity and specificity. In addition, we demonstrated that the formation of the ISMB/tRNA transcript complex requires more time than ISMB complex formation with unstructured short RNA.

Materials and Methods

Synthesis of ISMB molecules

Phosphoramidite monomers bearing fluorophore (pentamethyl indocarbocyanine, Cy3) and quencher (nitro methyl red) were synthesized as described previously^{22,23}. These monomers were directly used for the synthesis of ISMB via DNA/RNA synthesizer. ISMB molecules, consisting of DNA modified with Cy3 and nitro methyl red, were purchased from Tsukuba oligo service (Ibaraki, Japan). ISMBe and ISMBi target eMet and iMet, respectively. Sequences of ISMB molecules are shown in Table 1-1.

Table 1-1: Sequence of ISMBs

ISMB	Sequence
ISMBe1	5'-AFA <u>CCF TAC TGC GCT AAC GAG GCT</u> AQQ GGT QQT-3'
ISMBe2	5'-AFA <u>GAF TTA TGA GAC TGA CGC GCA</u> AQQ TCT QQT-3'
ISMBe3	5'-AFG <u>ACF CTT CAG ATT ATG AGA CTA</u> TQQ GTC QQT-3'
ISMBe4	5'-AFT <u>GGF TGC CCC GTG TGA GGA TCC</u> AQQ CCA QQT-3'
ISMBi1	5'-AFT <u>TCF CGC TGC GCC ACT CTG CCC</u> GQQ GAA QQT-3'
ISMBi2	5'-AFG <u>GGF TTA TGG GCC CAG CAC GCA</u> AQQ TCT QQT-3'
ISMBi3	5'-AFG <u>GAF CCT CTG GGT TAT GGG CCG</u> GQQ TCC QQT-3'
ISMBi4	5'-AFT <u>GGF TGG CAG AGG ATG GTT TCA</u> CQQCA QQT -3'
Scrambled ISMB	5'-AFG <u>TTF GAT GTG TTT AGT CGC TCT</u> CQQ AAC QQT-3'

Bases which hybridize with target sequence are underlined.

Preparation of eMet, iMet, and mutated eMet transcripts

For the study, eMet, iMet, and mutated eMet transcripts were prepared by in vitro transcription. To generate DNA templates for the transcription, primer extension was performed using 2 μ M of each primers (shown in Table 1-2) in a 100- μ l reaction mixture containing 0.2 mM dNTPs and 25 U KOD Dash DNA polymerase (Toyobo, Osaka, Japan), with the following temperature program: 94°C for 30 s; followed by 5 cycles of 94°C for 30 s, 55°C for 5 s, and 74°C for 30 s. The resultant template DNA was precipitated with 2-propanol. T7 RNA polymerase was produced in *Escherichia coli* BL21 pLysS (TaKaRa, Shiga, Japan) and purified on an Ni-NTA column (QIAGEN, Hilden, Germany). The Ni-NTA column was equilibrated with buffer A containing 50 mM Hepes-KOH (pH 7.6), 1 M NH_4Cl , 10 mM MgCl_2 , and 7 mM 2-mercaptethanol. T7 RNA polymerase was eluted by using a 20–500 mM imidazole gradient, and protein fractions were collected and analyzed by sodium dodecyl sulfate-polyacrylamide gel electrophoresis (SDS-PAGE). Fractions containing T7 RNA polymerase were dialyzed in buffer B containing 50 mM Hepes-KOH (pH 7.6), 100 mM KCl, 10 mM MgCl_2 , 7 mM 2-mercaptethanol, and 30% (v/v) glycerol. The transcription reaction was performed at 37°C for 5 h in a reaction mixture containing 40 mM Tris-HCl (pH 8.0), 24 mM MgCl_2 , 5 mM dithiothreitol, 10 mM GMP, 2 mM each of NTP, 1.8 U/ml inorganic pyrophosphatase (Sigma, St. Louis, MO, USA), 26.2 μ g/ml purified T7 RNA polymerase, and 10 μ g/ml DNA template. Finally, tRNA transcripts were purified by resolving on an

8% denaturing PAGE.

Table 1-2. Primer sequences used for preparing eMet, iMet and mutant eMet transcripts

Transcripts	Primers
eMet	(Forward) 5'-CGAAAT TAA TAC GAC TCA CTA TAG CCT CGT TAG CGC AGT AGG TAG CGC GTC AGT CTC ATA ATC-3' (Reverse) 5'-TGG TGC CCC GTG TGA GGA TCG AAC TCA CGA CCT TCA GAT TAT GAG ACT GAC GCG CTA C-3'
U8A	(Forward) 5'-CGA AAT TAA TAC GAC TCA CTA TAG CCT CGT AAG CGC AGT AGG TAG CGC GTC AGT CTC ATA ATC-3' (Reverse) 5'-TGG TGC CCC GTG TGA GGA TCG AAC TCA CGA CCT TCA GAT TAT GAG ACT GAC GCG CTA C-3'
U8AG12C	(Forward) 5'-CGA AAT TAA TAC GAC TCA CTA TAG CCT CGT AAG CCC AGT AGG TAG GGC GTC AGT CTC ATA ATC-3' (Reverse) 5'-TGG TGC CCC GTG TGA GGA TCG AAC TCA CGA CCT TCA GAT TAT GAG ACT GAC GCG CTA C-3'
U39A	(Forward) 5'-CGAAAT TAA TAC GAC TCA CTA TAG CCT CGT TAG CGC AGT AGG TAG CGC GTC AGT CTC ATA AAC-3' (Reverse) 5'-TGG TGC CCC GTG TGA GGA TCG AAC TCA CGA CCT TCA GTT TAT GAG ACT GAC GCG CTA C-3'
C34AU39A	(Forward) 5'-CGAAAT TAA TAC GAC TCA CTA TAG CCT CGT TAG

CGC AGT AGG TAG CGC GTC AGT CTA ATA ATC-3'

(Reverse) 5'-TGC CCC GTG TGA GGA TCG AAC TCA CGA CCT

TCA GAT TAT TAG ACT GAC GCG CTA C-3'

(Forward) 5'-CGAAAT TAA TAC GAC TCA CTA TAG CCT CGT TAG

G69A

CGC AGT AGG TAG CGC GTC AGT CTC ATA ATC-3'

(Reverse) 5'-TGG TGC CTC GTG TGA GGA TCG AAC TCA CGA

CCT TCA GAT TAT GAG ACT GAC GCG CTA C-3'

(Forward) 5'-CGAAAT TAA TAC GAC TCA CTA TAG CCT CGT TAG

G69AC64G

CGC AGT AGG TAG CGC GTC AGT CTC ATA ATC-3'

(Reverse) 5'-TGG TGC CTC GTG CGA GGA TCG AAC TCG CGA

CCTT CAG ATT ATG AGA CTG ACG CGC TAC-3'

(Forward) 5'-CGAAAT TAA TAC GAC TCA CTA TAG CCT CGT TAG

iMet

CGC AGT AGG TAG CGC GTC AGT CTC ATA ATC-3'

(Reverse) 5'-TGG TGC CCC GTG TGA GGA TCG AAC TCA CGA

CCT TCA GAT TAT GAG ACT GAC GCG CTA C-3'

Detection of eMet, iMet, and mutated eMet transcripts by ISMB

For the experiment, eMet or iMet transcripts (2 μ M) were renatured by incubating for 1 min at 85°C in buffer C containing 10 mM Tris-HCl (pH 8.0) and 2.5 mM MgCl₂, followed by slow cooling to 4°C. Renatured tRNA transcript (2 μ M) was incubated with 100 nM ISMBe or ISMBi in buffer C at 37°C for 2 h. Mutated eMet transcript (500 nM) was renatured and then incubated with 50 nM ISMBe. The fluorescence spectra of ISMB molecules were acquired at an excitation wavelength of 540 nm and an emission wavelength in the range of 550–700 nm using an FP-6600 spectrophotometer (JASCO, Tokyo, Japan). Excitation wavelength was set to \pm 5 nm bandwidth. To normalize the fluorescence intensities, completely digested 100 nM ISMBe1 was prepared as follows: ISMBe1 was incubated at 37°C for 30 min in a reaction mixture containing 10 mM Tris-HCl (pH 8.0), 2.5 mM MgCl₂, and 0.15 U/ml DNase I (Roche, Basel, Switzerland). Data are presented as the means \pm SEM of three independent experiments.

Time-dependent detection of eMet transcript and short RNA molecules by ISMBe

Renatured eMet transcript (2 μ M) or short RNA molecules were incubated with 100 nM ISMBe in buffer C at 37°C for 10–480 min. The fluorescence spectra were acquired as described above. Short RNA-1 (5'-GCC UCG UUA GCG CAG UAG GU-3'), short RNA-2 (5'-GCG CGU CAG UCU CAU AAU CU-3'), and short RNA-4 (5'-GAU CCU CAC ACG GGG CAC CA-3') were the same as sequences of each ISMBe target region

of eMet. These short RNAs were purchased from JBioS (Saitama, Japan). The fluorescence intensities were normalized to digested 100 nM ISMBe1. Data are presented as the means \pm SEM of three independent experiments.

Detection limit of ISMBe

Renatured eMet transcript (0–1000 nM) was incubated with 50 nM ISMBe in buffer C at 37°C for 2 h. The fluorescence spectra were acquired as described above. The limit of detection was determined by using the equation: detection limit = $[3 \times \text{standard deviation (average at 0 nM)}]/(\text{slope})$. The detection limit was calculated based on the linear range (0–500 nM eMet transcript), with concentrations of 1000 nM eMet excluded due to non-linearity. Data are presented as the means \pm SEM of three independent experiments.

Detection of the ISMBe1/tRNA transcript complex and endogenous eMet in living

HeLa cells

HeLa cells were obtained from RIKEN BRC which is participating the National Bio-Resource Project of the MEXT, Japan. HeLa cells were maintained in RPMI 1640 medium with 10% fetal bovine serum (Sigma) and 1% antibiotic-antimycotic solution (Gibco, Gaithersburg, MD, 2tUSA) at 37°C under an atmosphere of 5% CO₂. HeLa cells were plated on collagen-coated glass-based dish. After 2 d, the medium was exchanged for fresh medium without phenol red, and the cells were then microinjected with the reaction mixture specified below containing 20 μM Cy5 C5 maleimide (Thermo Fisher Scientific, Waltham, MA, USA) as an injection marker. For the experiment, 10 μM eMet or iMet transcripts was renatured by incubating for 1 min at 85°C in buffer D containing 20% Dulbecco's phosphate buffer saline (-) and 1 mM MgCl₂, followed by slow cooling to 4°C. Each renatured tRNA transcript (10 μM) was incubated with 1 μM ISMBe1 in buffer D at 37°C for 2 h. Microinjections were performed using Eppendorf Femtojet microinjection equipment (Eppendorf, Hamburg, Germany) and Femtotip microinjection capillary tips at 70 hPa. All imaging experiments were performed using an Olympus FV1200 confocal microscope (Olympus, Tokyo, Japan). The fluorescence intensities of ISMBe1 and Cy5 were quantified by using FV10-ASW 4.2 software (Olympus). Data are presented as the means ± SEM of four independent experiments. p-values were calculated using Student's t-test.

To detect endogenous eMet in living cells, the cells were microinjected with scrambled ISMB or ISMBe1. Imaging experiments were performed using an Olympus IX51 inverted microscope. The fluorescence intensities of scrambled ISMB and ISMBe1 were quantified using FV10-ASW 4.2 software. Data are the means \pm SEM of 7 cells for scrambled ISMB and 10 cells for ISMBe1.

Partial purification of mature eMet from HeLa cells

HeLa cells were grown until 70–80% confluence. The cells were suspended in solution D [4 M guanidium thiocyanate, 25 mM sodium citrate (pH 7.0), 0.5% sarcosyl, and 0.1 M 2-mercaptoethanol] for total RNA extraction. Proteins in the total RNA fraction were removed by phenol-saturated sodium acetate (pH 5.2). Total RNA was collected by precipitation with 2-propanol. It was then applied to a Q-Sepharose column (GE Healthcare, Hilden, Germany) equilibrated with buffer E containing 25 mM Tris-HCl (pH 7.4), 150 mM KCl, and 2.5 mM MgCl₂. Then, tRNA molecules were eluted with a linear gradient of KCl (0.3–2 M) in buffer E, and the fractions were analyzed by 7 M urea 8% PAGE. The eMet-specific radioisotope-labeled probe was prepared by using [γ -³²P]-ATP (PerkinElmer, Waltham, MA, USA) and T4 polynucleotide kinase (Toyobo). The sequence of the eMet-specific probe was as follows: 5'-ATT TTT GGT GCC CCG TGT GAG GAT CGA AC-3'. The tRNA mixture (2 μ g) containing each fraction eluted from Q-Sepharose was hybridized with 8.5 pmol eMet-specific radioisotope-labeled probe in

a buffer containing 10 mM Tris-HCl (pH 6.8) and 0.5 mM MgCl₂ for 10 min at 95°C, followed by slow cooling to 25°C. The reaction mixture was resolved on 8% native PAGE, and then eMet/probe complex was detected by using BIOMAX MS Film (Sigma). The fraction containing mature eMet was collected and the concentration of mature eMet was calculated using ImageJ software (Rasband, W.S., ImageJ, U. S. National Institutes of Health, Bethesda, MD, USA, <https://imagej.nih.gov/ij/>, 1997-2018), by comparison with the band intensity of 8.5 pmol eMet transcript/probe complex.

Detection of mature eMet by ISMBe

Renatured mature eMet (500 nM) was incubated with 50 nM ISMBe in buffer C at 37°C for 2 h. The fluorescence spectra were acquired as described above. Data are presented as the means ± SEM of three independent experiments.

Results

Detection of eMet and iMet transcripts by ISMB

Secondary structure of the eMet transcript was shown in Fig. 1-1A. To detect the eMet transcript, we designed four ISMBe molecules (Fig. 1-1A). ISMBe1 was targeted to the 5'-region, including the D arm; ISMBe2 was targeted to the anticodon arm, excluding the variable loop; ISMBe3 was targeted to the anticodon arm, including the variable loop; and ISMBe4 was targeted to the 3'-region including the T arm. To confirm that each ISMBe molecule detected the eMet transcript, the fluorescence intensities of ISMBe molecules were determined in the presence of eMet transcript. As shown in Fig. 1-1B, each ISMBe molecule could detect eMet transcript, with ISMBe1 showing the greatest fluorescence increase. In the absence of eMet transcript, the fluorescence intensities of ISMBe molecules remained at the background level. To investigate whether this behavior would also be observed with other tRNA molecules, we designed ISMB molecules to target iMet (ISMBi). The numerals of ISMBi correspond to the target region of ISMBe (Fig. 1-2A). As shown in Fig. 1-2B, ISMBi1 exhibited the highest sensitivity. These observations indicated that the target region including the D arm was the most suitable region for detecting a tRNA transcript by ISMB. On the other hand, the target region including the variable loop, such as ISMB3, was not suitable. Therefore, ISMBe molecules other than ISMBe3 were used in the subsequent analyses.

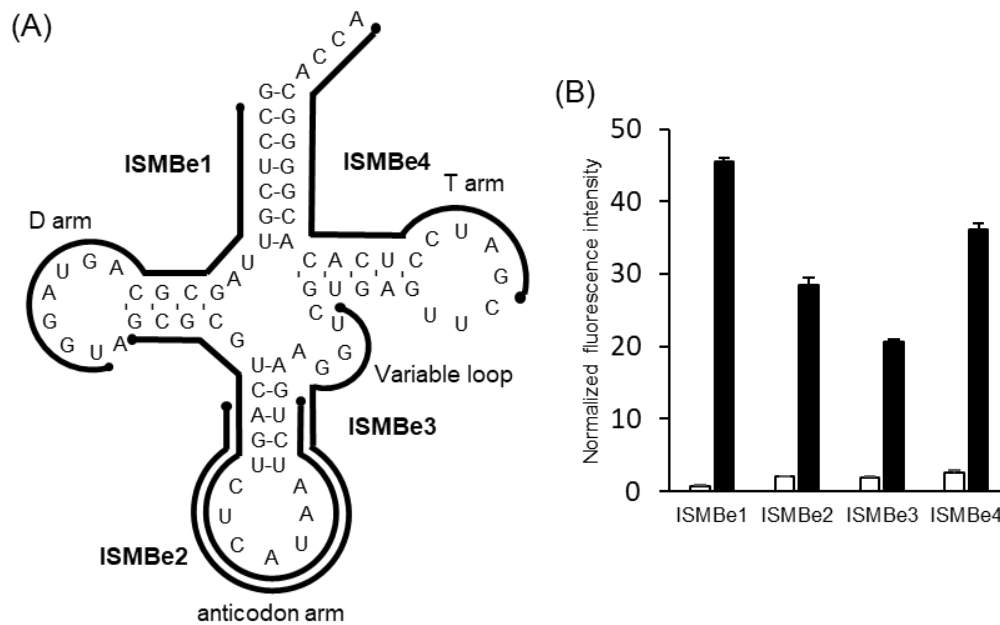


Figure 1-1. Detection of the eMet transcript by ISMBe. (A) The cloverleaf structure of eMet transcript is shown. Black lines are target regions of the designed ISMBe molecules. (B) The fluorescence intensities of ISMBe probes in the absence of target RNA (white bar) or in the presence of eMet transcript (black bar). The fluorescence intensities were normalized to digested ISMBe1. Data are the means \pm standard error of the mean (SEM) of three independent experiments.

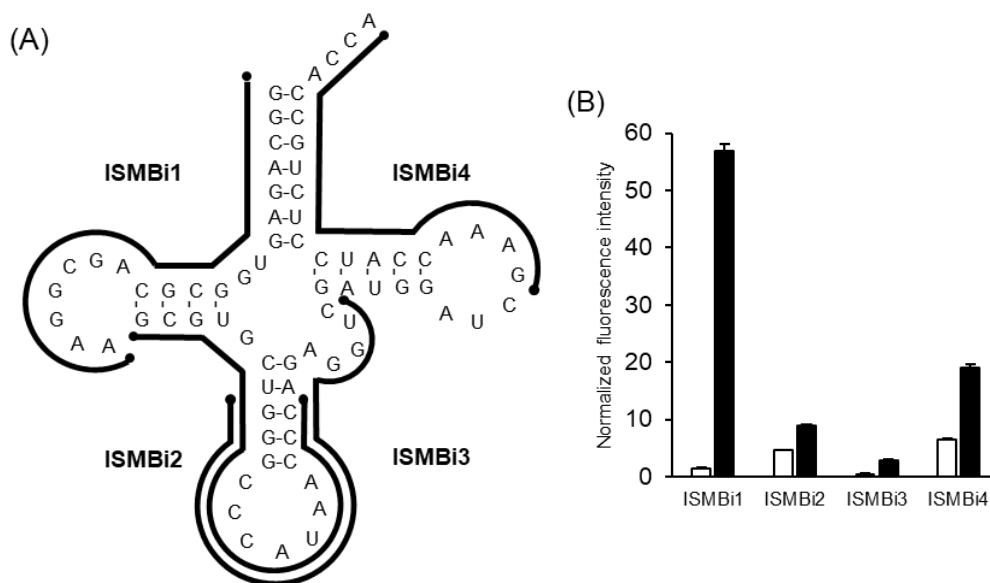


Figure 1-2. Detection of the iMet transcript by ISMBi. (A) The cloverleaf structure of eMet transcript is shown. Black lines are target regions of the designed ISMBi molecules. (B) The fluorescence intensities of ISMBi probes in the absence of target RNA (white bar) or in the presence of iMet transcript (black bar). The fluorescence intensities were normalized to digested ISMBi1. Data are the means \pm standard error of the mean (SEM) of three independent experiments.

Time-dependent increase of fluorescence intensity in the presence of eMet transcript or unstructured short RNA molecule

We previously showed that the fluorescence intensity of conventional MB in the presence of tRNA^{Lys3} transcript (15-min reaction) was lower than that of ISMBe and ISMBi in the presence of tRNA transcript (2-h reaction) (Fig. 1-1B and Fig. 1-2B)¹⁸. These observations suggested that the formation of the ISMBe/tRNA transcript complex requires a relatively long time. We reasoned that the binding of MB to tRNA molecules in a short period time could be difficult, as the latter are highly structured and typically do not have single-stranded regions. To test this working hypothesis, time-dependent fluorescence intensities of ISMBe were measured in the presence of the target RNA. The fluorescence intensities of ISMBe in the absence of the target RNA remained at the background level, with ISMBe quenched for 480 min (Fig. 1-3). In the presence of eMet transcript, the fluorescence intensities of ISMBe increased in a time-dependent manner and reached a plateau in 120 min (Fig. 1-3). By contrast, the fluorescence intensities of ISMBe reached a plateau already after 10 min in the presence of short RNA molecules (Short RNA-1, -2, -4), whose sequences were exactly the same as those of the target regions of eMet (Fig. 1-3). These observations suggested that ISMBe could rapidly hybridize with short RNA, as compared with the eMet transcript. As a consequence, the fluorescence increase in the presence of unstructured RNA was faster than that in the presence of tRNA transcript. In other words, these observations indicated that the

formation of the ISMB/RNA complex depends on the rigidity of RNA structure.

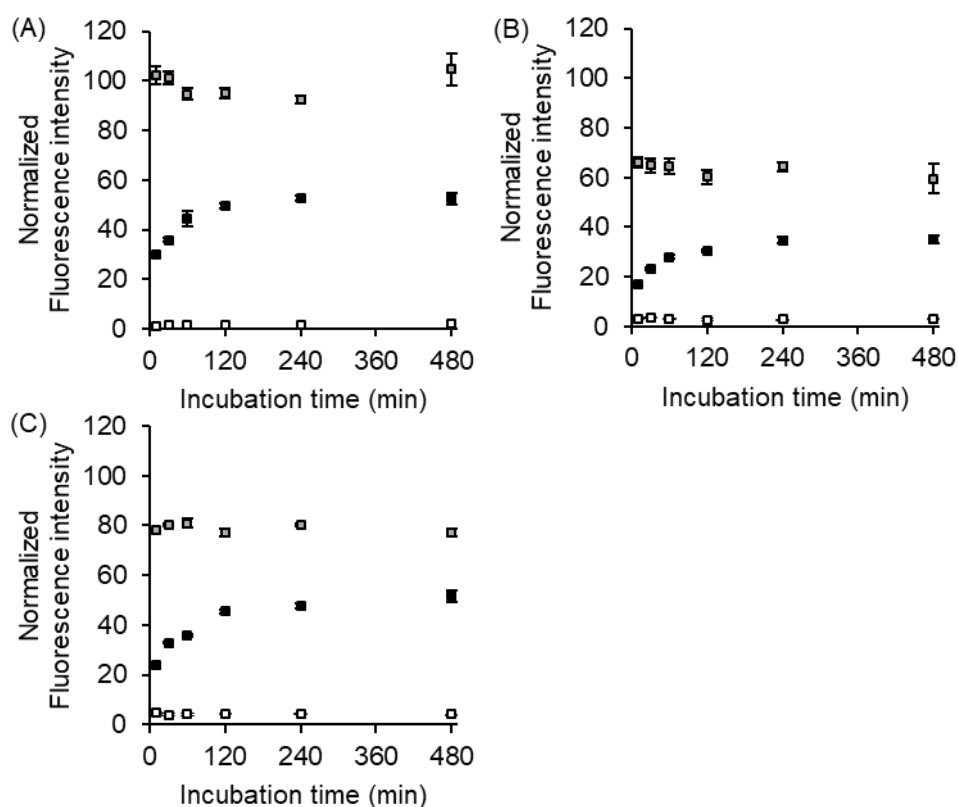


Figure 1-3. Time-dependent increase of the fluorescence intensity of ISMBe in the presence of the target RNA molecule. ISMBe1 (A), ISMBe2 (B), and ISMBe4 (C) were used in the experiments. The fluorescence intensities of ISMBe in the absence of target RNA (white), in the presence of short RNA (gray), and eMet transcript (black) are shown. The fluorescence intensities were normalized to digested ISMBe1. Data are the means \pm SEM of three independent experiments.

The detection limit of ISMBe1 and ISMBe4 is lower than that of ISMBe2

To determine the detection limit of ISMBe, the linearity of fluorescent response of each ISMBe molecule to a target transcript was examined. The fluorescence of each ISMBe molecule responded linearly to the increasing concentrations of the eMet transcript up to 500 nM (Fig. 1-4). The detection limit of ISMBe1 and ISMBe4 was 26.6 nM and 22.6 nM, respectively. The detection limit of ISMBe2 was 63.7 nM. These observations indicated that ISMBe1 and ISMBe4 were able to detect the eMet transcript with greater sensitivity than ISMBe2.

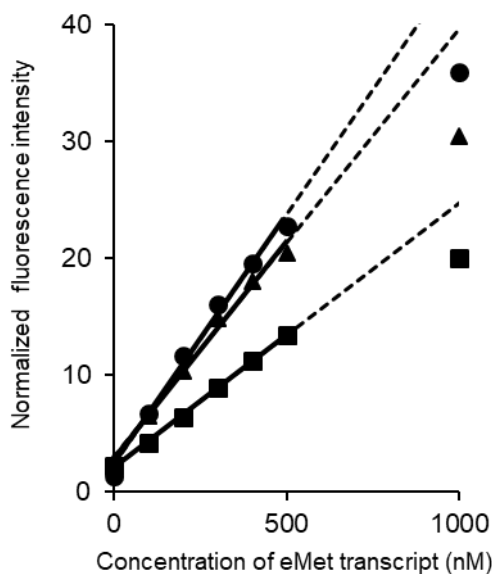


Figure 1-4. Detection limit of ISMBe molecules. ISMBe1 (circle), ISMBe4 (triangle), and ISMBe2 (square) were used in the experiments. Linear trendlines were plotted using the data points of fluorescence at 0–500 nM concentrations of the eMet transcript.

ISMBe specifically detects eMet transcript

To confirm that ISMBe specifically hybridized with the eMet transcript, eMet transcripts with one- and two-base mismatches were prepared (Fig. 1-5A). In addition, iMet transcript, which is accumulated in the nucleus after transfer from the cytoplasm, was also prepared as its sequence differs from that of eMet¹⁶. As shown in Fig. 1-5B-D, the fluorescence intensities of each ISMBe molecule in the presence of the iMet transcript and eMet transcripts with two-base mismatches (U8AG12C, C34AU39A, and G69AC64G) remained at the background level. Moreover, the fluorescence intensity of ISMBe4 increased only in the presence of the eMet transcript (Fig. 1-5D). On the other hand, the fluorescence intensity of ISMBe2 slightly increased in the presence of mutated transcript U39A, and the fluorescence intensity of ISMBe1 in the presence of mutated transcript U8A was similar to that in the presence of eMet transcript (Fig. 1-5B and C). These observations indicated that ISMBe4 was highly specific to eMet transcript.

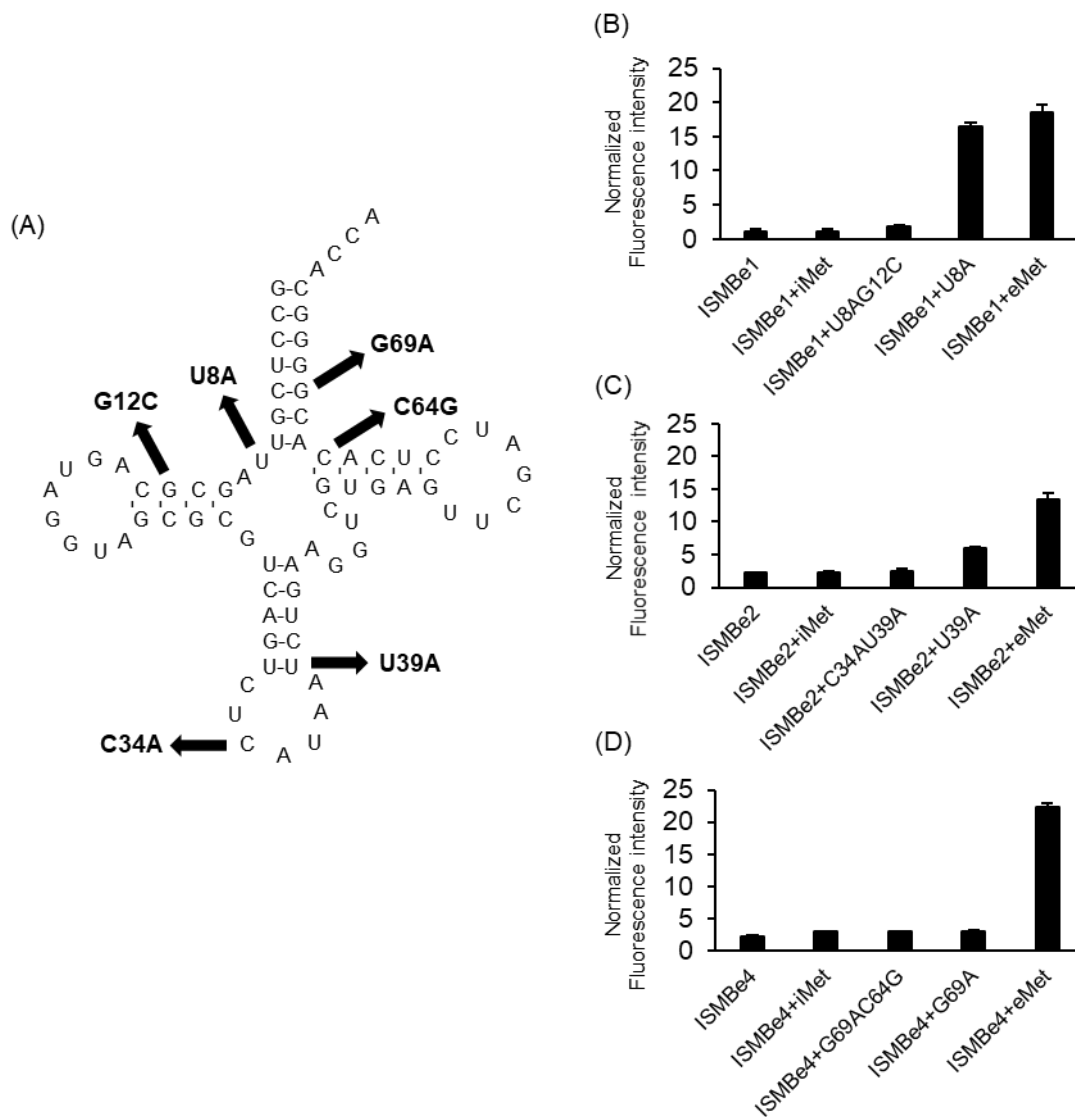


Figure 1-5. The specificity of ISMBe molecules. (A) Point mutations were individually introduced into the eMet transcript. The arrows indicate the mutation site and the substituted nucleotides. The fluorescence intensities of ISMBe1 (B), ISMBe2 (C), and ISMBe4 (D) in the presence of eMet transcript and mutated eMet transcripts are shown. Data are the means \pm SEM of three independent experiments.

Detection of the ISMBe1/eMet transcript complex in living HeLa cells

As shown in Fig. 1-1B, the signal background ratio of ISMBe1 was the highest. Therefore, ISMBe1 was initially used to detect endogenous eMet in living cells. To confirm the formation of a complex between ISMBe1 and the eMet transcript in living cells, ISMBe1 and eMet transcript were introduced into HeLa cells by microinjection. For the experiment, the iMet transcript was injected with ISMBe1 as a negative control. As shown in Fig. 1-6A and B, the fluorescence intensity of ISMBe1 in the cells after eMet transcript injection was significantly higher than that in cells after iMet transcript injection. This observation suggested that ISMBe1 is able to detect mature eMet in living HeLa cells.

To detect endogenous eMet in living cells, ISMBe1 and scrambled ISMB were introduced into HeLa cells by microinjection. The fluorescence intensities of ISMBe1 and scrambled ISMB in living cells were similar at 120 min (Fig. 1-7A). Next, time-dependent fluorescence intensities of ISMBe1 and scrambled ISMB were measured in living cells (Fig. 1-7B). The fluorescence intensities of both molecules increased to a similar extent in a time-dependent manner at similar level in living cells. However, the fluorescence intensity of ISMBe1 in the absence of the target RNA remained at background levels until 480 min (Fig. 1-3A), indicating that ISMB may be degraded in living cells.

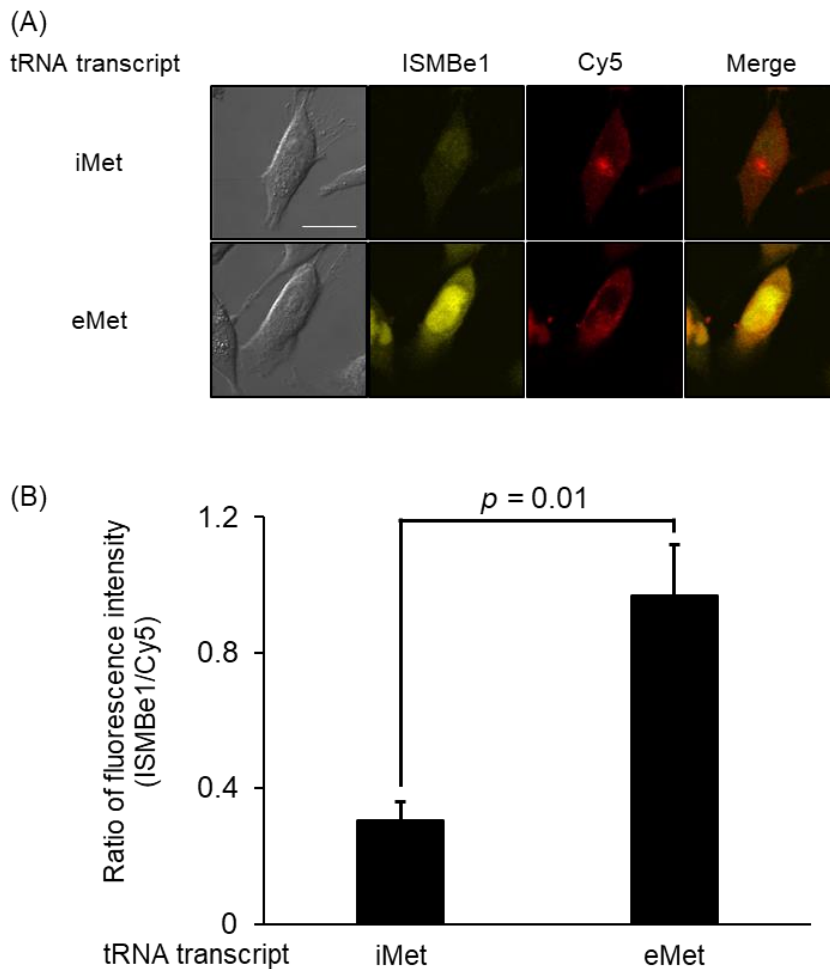


Figure 1-6. Detection of the ISMBe1/eMet transcript complex in living cells. (A) Detection of the ISMBe1/eMet transcript complex in living cells, with Cy5 introduced as an injection marker. (B) The fluorescence intensity ratio of ISMBe1 in the presence of iMet transcript (left) and in the presence of eMet transcript (right). The fluorescence intensities were normalized to Cy5. Scale bar, 20 μ m. Data are the means \pm SEM of four independent experiments. More than 6 cells were measured in each experiment. p-values were calculated using Student's t-test.

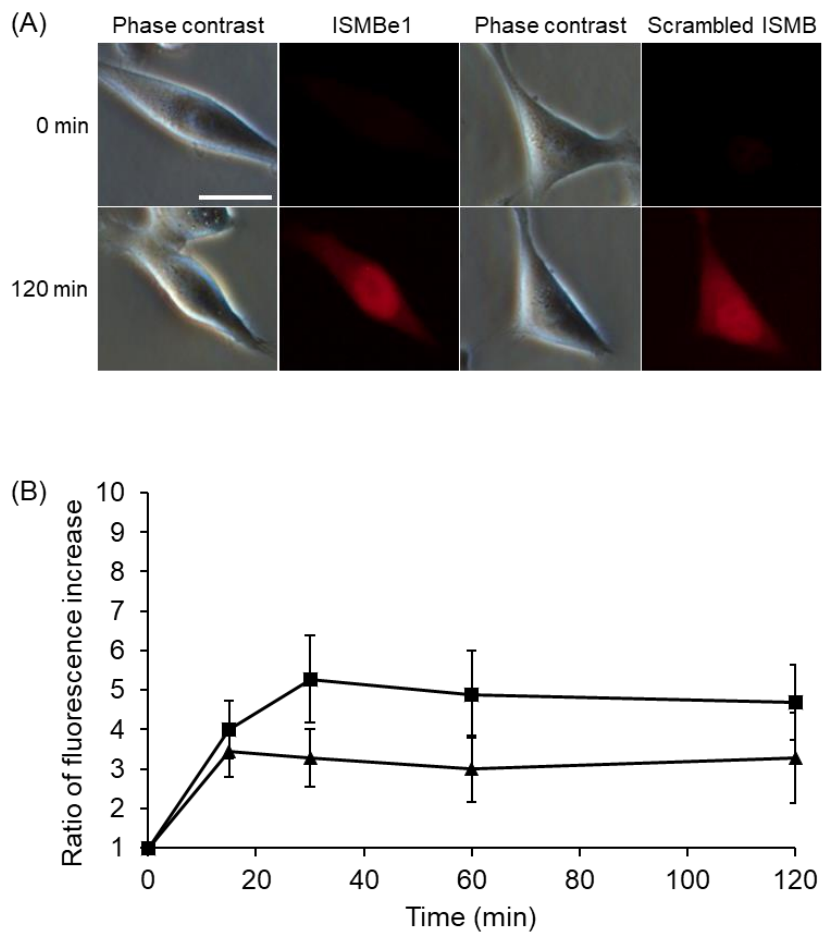


Figure 1-7. Detection of the ISMBe1 in living cells. (A) Image of living cells injected ISMB at 120 min. (B) Increase in the fluorescence of scrambled ISMB (square) and ISMBe1 (triangle) in living cells are shown. Fluorescence intensity of each cell at 0 min was defined as 1.0. Data are the means \pm SEM of 7 cells for scrambled ISMB and 10 cells for ISMBe1. Scale bar, 20 μ m.

ISMBe detects mature eMet

We were concerned that multiple nucleotide modifications of mature eMet might interfere with the hybridization of ISMBe1 and mature eMet (Fig. 1-9A), since the presence of modified nucleotides in tRNA interferes with the hybridization of a DNA array probe and tRNA²⁴. To address this question, we initially prepared partially purified mature eMet from HeLa cells. Total RNA from HeLa cells was fractionated by anion-exchange chromatography and tRNA molecules in each fraction were detected by electrophoresis. We observed that tRNA molecules were present in fractions 13–16 (Fig. 1-8). To identify the fraction that contained mature eMet, eMet-specific radioisotope-labeled probe was used. The eMet/probe complex was detected only in fraction 13, indicating that mature eMet was contained in that fraction (Fig. 1-8B).

To investigate whether ISMBe could detect mature eMet, the fluorescence intensities of ISMBe molecules were determined in the presence of mature eMet from fraction 13. The fluorescence intensity of scrambled ISMB in the presence of mature eMet remained at the background level (Fig. 1-9B). The fluorescence intensities of ISMBe molecules in the presence of mature eMet increased, with ISMBe1 exhibiting the highest fluorescence increase. However, the increase of fluorescence of ISMBe molecules in the presence of mature eMet was lower than that of ISMBe molecules in the presence of eMet transcript (Fig. 1-1B and 1-9B). These observations indicated that ISMBe molecules can be used to detect mature eMet, however, modified nucleotides impact the hybridization of ISMBe

molecules and mature eMet.

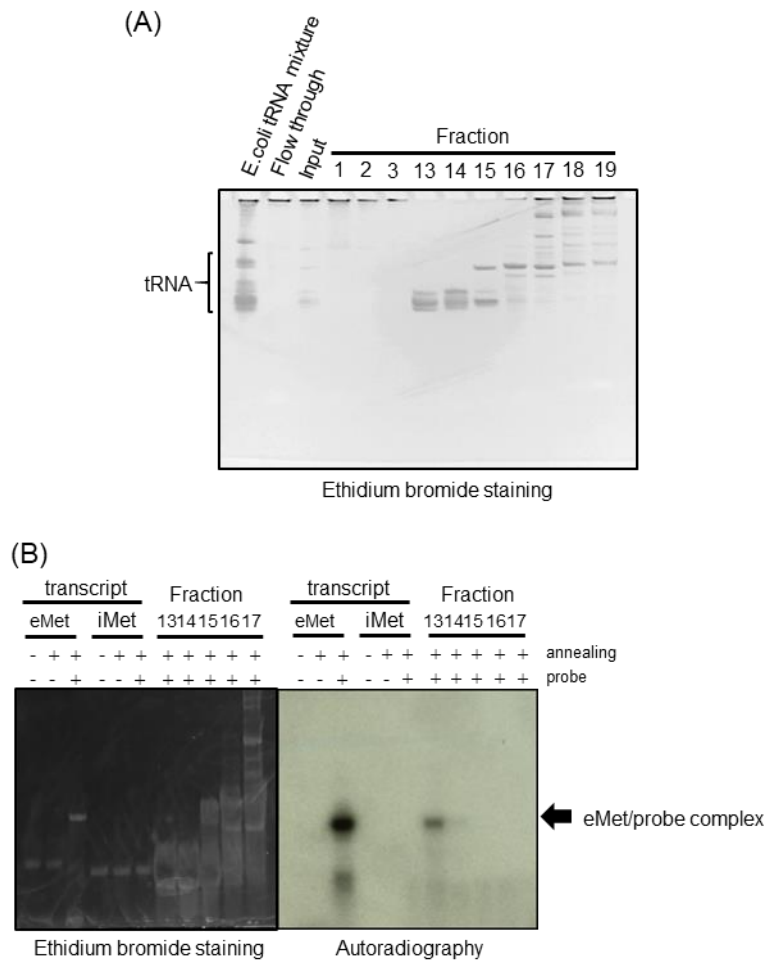


Figure 1-8. Purification of mature eMet. (A) After anion exchange chromatography, each fraction was analyzed by 7 M urea 8% PAGE. (B) The complex of eMet with eMet-specific radioisotope-labeled probe was electrophoresed on 8% native PAGE, and was then detected by ethidium bromide staining (left) and by autoradiography (right).

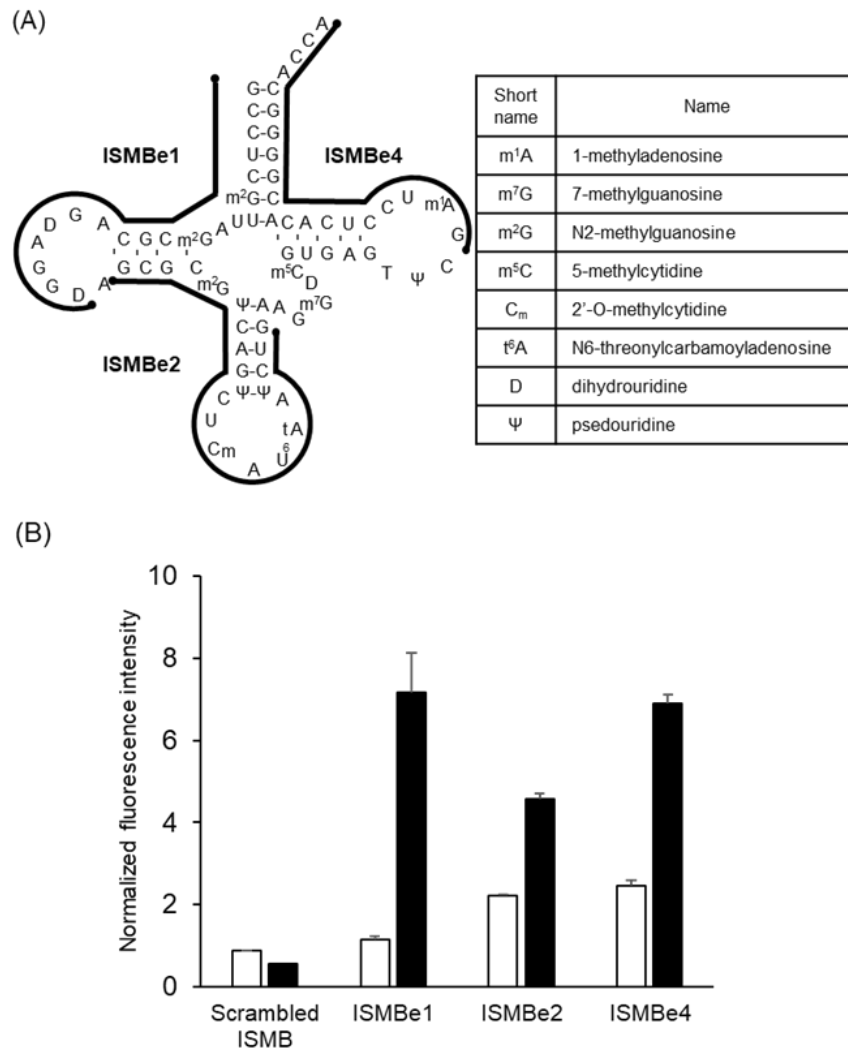


Figure 1-9. Detection of mature eMet by ISMBe. (A) The cloverleaf structure of mature eMet is shown 25. (B) The fluorescence intensities of ISMBe molecules in the absence of target RNA (white) and in the presence of mature eMet (black). The fluorescence intensities were normalized to digested ISMBe1. Data are the means \pm SEM of three independent experiments.

Discussion

In the current study, to determine the effective target region of ISMB for detecting tRNA molecules, eight ISMB molecules targeted to the representative tRNA regions were designed. We showed that ISMBe molecules, particularly ISMBe1, targeted to the 5'-region inclusive of the D arm, could be used to detect eMet transcript and mature eMet (Fig. 1-1 and 1-9). In addition, ISMBi1, targeted to the 5'-region inclusive of the D arm, similarly detected the iMet transcript with higher sensitivity than the other ISMBi probes (Fig. 1-2B). These observations indicated that ISMB targeted to the 5'-region, inclusive of the D arm, detected tRNA with high sensitivity.

To determine whether the sensitivity of ISMB molecules depends on the stability of the ISMB/tRNA complex, we calculated the free energy (ΔG) of each ISMBe and ISMBe/eMet transcript complex using the RNAstructure 5.3 software (Table 3)^{26,27}. The predicted free energies were the same, indicating lack of correlation between the sensitivity of ISMB and the stability of the ISMBe/eMet transcript complex. In a previous study, we showed that conventional MB molecules targeted to the D arm more sensitively detect tRNA^{Lys3} transcript than those targeted to the anticodon arm and the T arm¹⁸. Furthermore, according to thermal unfolding studies, the D arm is more readily melted than other regions^{28,29}. This indicated that ISMB most readily hybridizes with the D arm.

Previously, we showed that the fluorescence increase of conventional MB targeted to the T arm, excluding the CCA sequence, is the lowest among the analyzed probes

targeting various tRNA regions¹⁸. On the other hand, the fluorescence increases of ISMBe4 and ISMBi4 molecules targeted to the T arm, including the CCA sequence, in the presence of eMet and iMet transcript, respectively, were higher than those of ISMBe2 and ISMBi2 targeted to the anticodon arm, respectively (Fig. 1-1B and 1-2B). Furthermore, the detection limit of ISMBe1 and ISMBe4 was almost the same (Fig. 1-4). Although the tRNA molecule is highly structured, the CCA sequence of tRNA is unfolded and forms a short single-stranded region. As shown in Fig. 1-3, ISMBe could rapidly hybridize with short RNA. Collectively, these observations suggested that ISMBe4 initially hybridizes with the CCA sequence of tRNA and then hybridizes with the target sequence of the T arm region of tRNA.

As shown in Fig. 1-1, 1-3, and 1-9, the formation of the ISMB/RNA complex depends on the rigidity of RNA structure, and the modified nucleotides of mature eMet impact the hybridization of ISMBe and mature eMet. Data shown in Fig. 1-1 and 1-9 indicate an additional possibility. In general, the modified nucleotides on tRNA contribute to the thermal stability of tRNA³⁰. For instance, mature tRNA^{Asp} (T_m=73°C) from yeast is more stable than the tRNA^{Asp} transcript (T_m=65°C)³¹. Therefore, the hybridization of ISMBe and mature eMet might be inhibited relative to that of the ISMBe and eMet transcript, since eMet transcript melts more easily than mature eMet.

The current study highlights some limitations of the devised method. First, ISMBe1 and ISMBe2 detected eMet transcripts with one-base mismatches (Fig. 1-5B and C). In

addition, multiple modified nucleotides on a mature tRNA molecule affected the hybridization of ISMB and mature tRNA (Fig. 1-9). Moreover, we found that ISMB may be degraded in living cells (Fig. 1-7). These issues might be addressed by designing ISMB based on other structural backbones, such as locked nucleic acids (LNAs), peptide nucleic acids (PNAs) and serinol nucleic acids (SNAs) which introduces 2,6-diaminopurine³²⁻³⁷. LNA-, PNA-, and SNA-based probes can bind to double-stranded RNA with high affinity and high specificity. Furthermore, these probes are resistant to most enzymes, such as DNase and RNase. Therefore, LNA-, PNA-, or SNA- based ISMB probes may be able to detect endogenous tRNA in living cells without being degraded.

In summary, we demonstrated that ISMB targeted to the D arm region is the most suitable probe for detecting tRNA transcripts and mature tRNA. While the ISMB/short RNA complex was rapidly formed, the formation of the tRNA/ISMB complex required a relatively long time. Until now, tRNA localization has been mainly analyzed by the FISH method and fluorescence labeling of tRNA in mammalian cells^{14,16,17,38-40}, and tRNA levels are mainly analyzed by northern blotting^{14,41}. Therefore, endogenous tRNA molecules have been not yet observed in living mammalian cells. In the future, ISMB, after the above-mentioned issues have been resolved, may be used to detect endogenous tRNA in living mammalian cells. ISMB-based tRNA detection and tRNA localization analysis in mammalian cells exposed to environmental stresses and chemical reagents may constitute a useful tool for various biological and medical applications.

Table 1-3. ΔG (kcal mol⁻¹) of each ISMBe and ISMBe/eMet transcript complex

	ΔG of ISMB	ΔG of ISMB/eMet transcript complex
ISMBe1	-7.1	-54.1
ISMBe2	-2.0	-50.0
ISMBe3	-2.6	-52.8
ISMBe4	-8.6	-50.5
ISMBi1	-7.5	-58.4
ISMBi2	-6.0	-57.1
ISMBi3	-10.5	-61.4
ISMBi4	-6.2	-57.8

References

- (1) Ryder PV, Lerit DA. (2018) RNA localization regulates diverse and dynamic cellular processes. *Traffic*. 19, 496–502.
- (2) Olde Loohuis NFM, Kos A, Martens GJM, Van Bokhoven H, Nadif Kasri N, Aschrafi A. (2012) MicroRNA networks direct neuronal development and plasticity. *Cell Mol Life Sci* 69, 89–102.
- (3) Watanabe K, Yamaji R, Ohtsuki T. (2018) MicroRNA-664a-5p promotes neuronal differentiation of SH-SY5Y cells. *Genes Cells*. 23, 225–233.
- (4) Crino PB, Eberwine J. (1996) Molecular characterization of the dendritic growth cone: regulated mRNA transport and local protein synthesis. *Neuron*. 17, 1173–1187.
- (5) Doyle M, Kiebler MA. (2011) Mechanisms of dendritic mRNA transport and its role in synaptic tagging. *EMBO J*. 30, 3540–3552.
- (6) Chan JF-W, Yip CC-Y, Tee K-M, Zhu Z, Tsang JO-L, Chik KK-H, Tsang TG-W, et al. (2017) Improved detection of Zika virus RNA in human and animal specimens by a novel, highly sensitive and specific real-time RT-PCR assay targeting the 5'-untranslated region of Zika virus. *Trop Med Int Heal*. 22, 594–603.
- (7) Schwarzer A, Emmrich S, Schmidt F, Beck D, Ng M, Reimer C, Adams FF, et al. (2017) The non-coding RNA landscape of human hematopoiesis and

- leukemia. *Nat Commun.* 8, 1–16.
- (8) Lécuyer E, Yoshida H, Parthasarathy N, Alm C, Babak T, Cerovina T, Hughes TR, et al. (2007) Global analysis of mRNA localization reveals a prominent role in organizing cellular architecture and function. *Cell.* 131, 174–187.
- (9) Santangelo PJ, Nix B, Tsourkas A, Bao G. (2004) Dual FRET molecular beacons for mRNA detection in living cells. *Nucleic Acids Res.* 32, 1–9.
- (10) Ma Z, Wu X, Krueger CJ, Chen AK. (2017) Engineering novel molecular beacon constructs to study intracellular RNA dynamics and localization. *Genomics Proteomics Bioinforma.* 15, 279–286.
- (11) Tyagi S, Kramer FR. (1996) Molecular beacons: probes that fluoresce upon hybridization. *Nat Biotechnol.* 14, 303–308.
- (12) Baker MB, Bao G, Searles CD. (2012) In vitro quantification of specific microRNA using molecular beacons. *Nucleic Acids Res.* 40, 1–12.
- (13) Bohländer PR, Abba ML, Bestvater F, Allgayer H, Wagenknecht HA. (2016) Two wavelength-shifting molecular beacons for simultaneous and selective imaging of vesicular miRNA-21 and miRNA-31 in living cancer cells. *Org Biomol Chem.* 14, 5001–5006.
- (14) Watanabe K, Miyagawa R, Tomikawa C, Mizuno R, Takahashi A, Hori H, Ijiri K. (2013) Degradation of initiator tRNA^{Met} by Xrn1/2 via its accumulation in the nucleus of heat-treated HeLa cells. *Nucleic Acids Res.* 41, 4671–4685.

- (15) Watanabe K, Ijiri K, Ohtsuki T. (2014) mTOR regulates the nucleoplasmic diffusion of Xrn2 under conditions of heat stress. *FEBS Lett.* 588, 3454–3460.
- (16) Miyagawa R, Mizuno R, Watanabe K, Ijiri K. (2012) Formation of tRNA granules in the nucleus of heat-induced human cells. *Biochem Biophys Res Commun.* 418, 149–155.
- (17) Barhoom S, Kaur J, Cooperman BS, Smorodinsky NI, Smilansky Z, Ehrlich M, Elroy-Stein O, et al. (2011) Quantitative single cell monitoring of protein synthesis at subcellular resolution using fluorescently labeled tRNA. *Nucleic Acids Res.* 39, e129.
- (18) Li J, Xu C, Shimada N, Miyoshi Y, Watanabe K, Cong W, Ohtsuki T, et al. (2017) Detection of small, highly structured RNAs using molecular beacons. *Anal Methods.* 9, 2971–2976.
- (19) Kashida H, Takatsu T, Fujii T, Sekiguchi K, Liang X, Niwa K, Takase T, et al. (2009) In-stem molecular beacon containing a pseudo base pair of threoninol nucleotides for the removal of background emission. *Angew Chem Int Ed Engl.* 48, 7044–7047.
- (20) Hara Y, Fujii T, Kashida H, Sekiguchi K, Liang X, Niwa K, Takase T, et al. (2010) Coherent quenching of a fluorophore for the design of a highly sensitive in-stem molecular beacon. *Angew Chem Int Ed Engl.* 49, 5502–5506.
- (21) Asanuma H, Osawa T, Kashida H, Fujii T, Liang X, Niwa K, Yoshida Y, et al.

- (2012) A polycation-chaperoned in-stem molecular beacon system. *Chem Commun.* 48, 1760–1762.
- (22) Kashida H, Osawa T, Morimoto K, Kamiya Y, Asanuma H. (2015) Molecular design of Cy3 derivative for highly sensitive in-stem molecular beacon and its application to the wash-free FISH. *Bioorg Med Chem.* 23, 1758–1762.
- (23) Fujii T, Kashida H, Asanuma H. (2009) Analysis of coherent heteroclustering of different dyes by use of threoninol nucleotides for comparison with the molecular exciton theory. *Chemistry.* 15, 10092–10102.
- (24) Hiley SL, Jackman J, Babak T, Trochesset M, Morris QD, Phizicky E, Hughes TR. (2005) Detection and discovery of RNA modifications using microarrays. *Nucleic Acids Res.* 33, e2.
- (25) Farruggio D, Chaudhuri J, Maitra U, RajBhandary UL. (1996) The A1 x U72 base pair conserved in eukaryotic initiator tRNAs is important specifically for binding to the eukaryotic translation initiation factor eIF2. *Mol Cell Biol.* 16, 4248–4256.
- (26) Mathews DH, Disney MD, Childs JL, Schroeder SJ, Zuker M, Turner DH. (2004) Incorporating chemical modification constraints into a dynamic programming algorithm for prediction of RNA secondary structure. *Proc Natl Acad Sci USA.* 101, 7287–7292.
- (27) Reuter JS, Mathews DH. (2010) RNAstructure: software for RNA secondary

- structure prediction and analysis. *BMC Bioinformatics*. 11, 129.
- (28) Rhodes D. (1977) Initial stages of the thermal unfolding of yeast phenylalanine transfer RNA as studied by chemical modification: the effect of magnesium. *Eur J Biochem*. 81, 91–101.
- (29) Wilkinson KA, Merino EJ, Weeks KM. (2005) RNA shape chemistry reveals nonhierarchical interactions dominate equilibrium structural transitions in tRNA(Asp) transcripts. *J Am Chem Soc*. 127, 4659–4667.
- (30) Hori H. (2014) Methylated nucleosides in tRNA and tRNA methyltransferases. *Front Genet*. 5, 1–26.
- (31) Perret V, Garcia A, Puglisi J, Grosjean H, Ebel JP, Florentz C, Giegé R, (1990) Conformation in solution of yeast tRNA(Asp) transcripts deprived of modified nucleotides. *Biochimie*. 72, 735–743.
- (32) Hagedorn PH, Persson R, Funder ED, Albæk N, Diemer SL, Hansen DJ, Møller MR, et al. (2018) Locked nucleic acid: modality, diversity, and drug discovery. *Drug Discov Today*. 23, 101–114.
- (33) Yang CJ, Wang L, Wu Y, Kim Y, Medley CD, Lin H, Tan W. (2007) Synthesis and investigation of deoxyribonucleic acid/locked nucleic acid chimeric molecular beacons. *Nucleic Acids Res*. 35, 4030–4041.
- (34) Vilaivan T. (2018) Fluorogenic PNA probes. *Beilstein J Org Chem*. 14, 253–281.
- (35) Li M, Zengeya T, Rozners E. (2010) Short peptide nucleic acids bind strongly to

- homopurine tract of double helical RNA at pH 5.5. *J Am Chem Soc.* 132, 8676–8681.
- (36) Murayama K, Kamiya Y, Kashida H, Asanuma H. (2015) Ultrasensitive molecular beacon designed with totally Serinol Nucleic Acid (SNA) for monitoring mRNA in cells. *Chembiochem.* 16, 1298–1301.
- (37) Kamiya Y, Donoshita Y, Kamimoto H, Murayama K, Ariyoshi J, Asanuma H. (2017) Introduction of 2,6-diaminopurines into serinol nucleic acid improves anti-miRNA performance. *Chembiochem.* 18, 1917–1922.
- (38) Shaheen HH, Horetsky RL, Kimball SR, Murthi A, Jefferson LS, Hopper AK. (2007) Retrograde nuclear accumulation of cytoplasmic tRNA in rat hepatoma cells in response to amino acid deprivation. *Proc Natl Acad Sci USA.* 104, 8845–8850.
- (39) Chafe SC, Pierce JB, Eswara MBK, McGuire AT, Mangroo D. (2011) Nutrient stress does not cause retrograde transport of cytoplasmic tRNA to the nucleus in evolutionarily diverse organisms. *Mol Biol Cell.* 22, 1091–1103.
- (40) Liu J, Pampillo M, Guo F, Liu S, Cooperman BS, Farrell I, Dahary D, et al. (2014) Monitoring collagen synthesis in fibroblasts using fluorescently labeled tRNA pairs. *J Cell Physiol.* 229, 1121–1129.
- (41) Okamoto M, Fujiwara M, Hori M, Okada K, Yazama F, Konishi H, Xiao Y, et al. (2014) tRNA modifying enzymes, NSUN2 and METTL1, determine sensitivity

to 5-fluorouracil in HeLa cells. *PLoS Genet.* 10, e1004639.

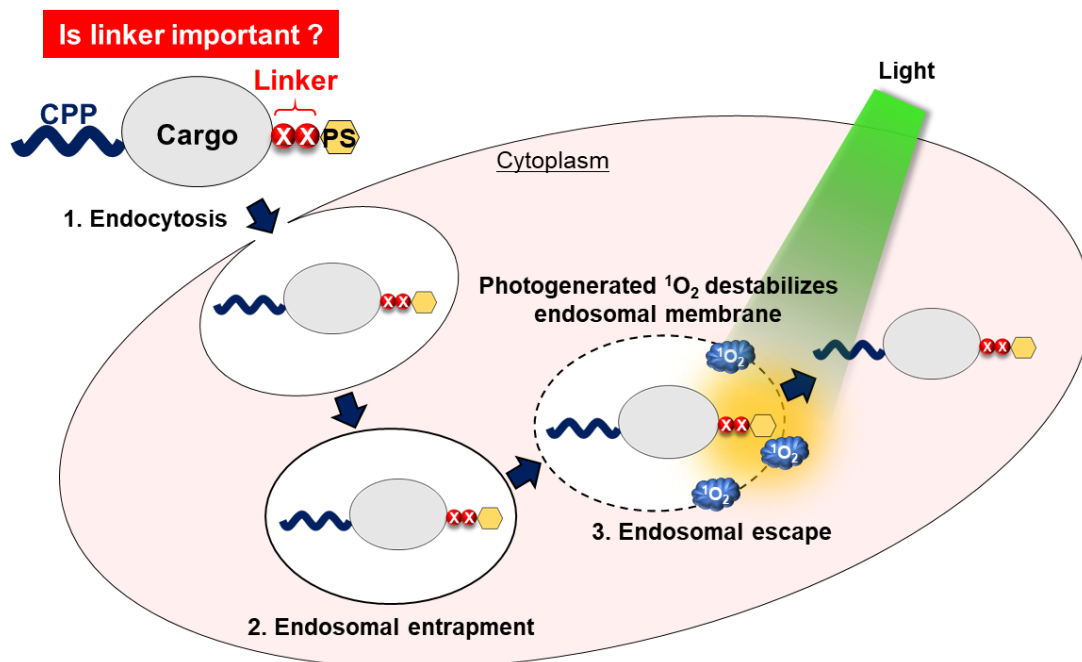
Chapter 2

Endosomal escape of peptide-photosensitizer conjugates is
affected by amino acid near the photosensitizer

Abstract

Cell-penetrating peptides (CPPs) are widely used for the intracellular delivery of peptides and proteins, but CPP fusion peptides and proteins are often transported by endocytosis and trapped in endosomes. Photochemical internalization (PCI) is a method for the endosomal escape of the trapped peptide or protein and release into the cytosol using light and photosensitizers. In PCI, endosomal membranes are thought to be destabilized by singlet oxygen ($^1\text{O}_2$) photogenerated from photosensitizers localized in endosomes. We previously developed CPP-cargo-photosensitizer (PS) conjugates able to photo-dependently enter the cytosol via the PCI mechanism. For example, TatU1A-PS (a covalent complex of Tat [CPP], U1A RNA-binding protein [cargo], and PS) can photo-dependently deliver RNAs into the cytosol, and TatBim-PS (a covalent complex of Tat, Bim [cargo], and PS) can photoinduce apoptosis in mammalian cells. However, for many newly created conjugates, the induction of PCI has been insufficient. We hypothesized that the amino acid linker sequence (XX) adjacent to the photosensitizer are an important determinant of PCI efficiency. In this study, using CPP-cargo-XX-PS platforms, we examined the relationship between PCI efficiency and the linker amino acid sequence near the photosensitizer. We found that hydrophobic FF and LL linkers enhanced the PCI efficiencies of both TatBim-XX-PS and TatU1A-XX-PS. The effectiveness of the linker depended, in part, on both the cargo moiety and the photosensitizer. These results may guide the design of CPP-cargo-PS conjugates conferring broad target functions for PCI

and photodynamic therapy.



Graphical abstract of this study

Introduction

Conjugation to cell-penetrating peptides (CPPs) is a general method for the delivery of functional proteins and peptides into cells¹⁻³. However, many CPP-mediated protein/peptide delivery strategies result in endosomal entrapment⁴⁻⁶. Photochemical internalization (PCI) is a promising method for the release of trapped molecules into the cytosol using light and photosensitizers⁷⁻⁹. In this method, endosomal membranes are destabilized by singlet oxygen ($^1\text{O}_2$) photogenerated from photosensitizers¹⁰⁻¹³. The use of CPP-photosensitizer conjugates has also been studied for the PCI of macromolecular therapeutics and nanoparticles¹⁴⁻¹⁷. An important aspect of the conjugation of photosensitizers and peptides (CPPs and CPP-fusion peptides) is that this approach can repurpose peptides that would otherwise be unsuitable for PCI applications¹⁶.

To enable the CPP- and PCI-mediated cytosolic delivery of functional protein/peptide cargoes, we have previously developed CPP-cargo-photosensitizer (PS) conjugates, including TatU1A-PS^{11,18-20} and TatBim-PS⁶. TatU1A-PS is a conjugate of the fusion protein of HIV TAT-derived CPP, human U1A-derived RNA-binding protein, and a photosensitizer. Several dyes, such as Alexa Fluor 546 (Alexa546) and DY750, could be used as the PS moiety of TatU1A-PS^{19,21}. TatU1A-PS could photo-dependently deliver RNAs into the cytosol. TatBim-Alexa546 is a conjugate of HIV TAT-derived CPP, the BH3 domain derived from Bim, an apoptosis-inducing protein, and the photosensitizer Alexa546. This conjugate could photoinduce apoptosis.

Although most of the failed results were not reported, many of the CPP-cargo-PS conjugates developed by our group did not sufficiently induce PCI¹⁸. Even with identical CPPs and photosensitizers, CPP-cargo-PS conjugates sometimes result in insufficient PCI, suggesting that the properties of cargoes affect PCI efficiency. In particular, the amino acid sequence near the photosensitizer is highly likely to affect efficiency. The photosensitizing properties of chlorin derivatives are affected by the functional groups on chlorin^{22,23}. Smith et al. have synthesized various chlorin-e₆-bis(amino acid) conjugates and demonstrated that the bis(amino acid) modifications affect the cellular localization and phototoxicities of the modified chlorin e₆²³. Additionally, modified porphyrins have different ¹O₂ quantum yields in liposomes, with a difference of up to 1.44-fold among porphyrin derivatives²⁴, and the ¹O₂ quantum yields of modified eosins can differ up to 1.82-fold⁵. These reports suggest that the optimization of modification of a photosensitizer, which can be an amino acid sequence near the photosensitizer, can improve the efficiency of PCI.

In this study, using CPP-cargo-linker-PS platforms (Fig. 2-1), we examined the relationship between PCI efficiency and the linker amino acid sequence near the photosensitizer. In particular, we used TatU1A-PS and TatBim-PS with a linker between the cargo and photosensitizer. Since it is difficult to comprehensively evaluate linkers (e.g., there are 20 possible 1-amino acid (aa) linkers, 400 possible 2-aa linkers, 8000 possible 3-aa linkers, and so on), we focused on 2-aa linkers with a repeat of a specific

amino acid (XX linkers). XX linkers were chosen instead of 1-aa X linkers because the amino acid characteristics (such as hydrophobicity and acidity) seem to be enhanced by the repeat. We examined thirteen XX linkers, including hydrophobic (X = A, F, L, V, W), acidic (D, E), basic (K, R, H), and polar (G, N, S) amino acids.

Our focus was to evaluate the effectiveness of XX linker for the photoinduced endosomal escape of CPP-cargo-XX-PS molecules. This will guide the future design of CPP-cargo-PS conjugates with various cargoes for efficient PCI. As CPP-cargo-linker-PS platforms, we used TatBim-XX-Alexa546, TatBim-XX-eosin, and TatU1A-XX-Alexa546. Two different cargoes (Bim and U1A) and two different photosensitizers (Alexa546 and eosin) were used. Although Alexa546 and eosin are not the most commonly used photosensitizers, eosin has been used for this purpose in many photodynamic therapy (PDT) or PCI studies²⁵⁻²⁷, and we have used Alexa546 in our PCI studies^{11, 28}. Thiol-reactive photosensitizers, such as eosin-maleimide, are necessary for the syntheses of CPP-cargo-PS conjugates. The most common, standard PCI photosensitizers, such as TPPS_{2a} and AlPcS_{2a}, cannot be easily used for the synthesis, because TPPS_{2a}- and AlPcS_{2a}-maleimide are not commercially available. We also compared ¹O₂ quantum yields of short peptide-eosin conjugates including the XX linker (XX-eosin series) to investigate the influence of linker amino acids on the photophysical properties of eosin.

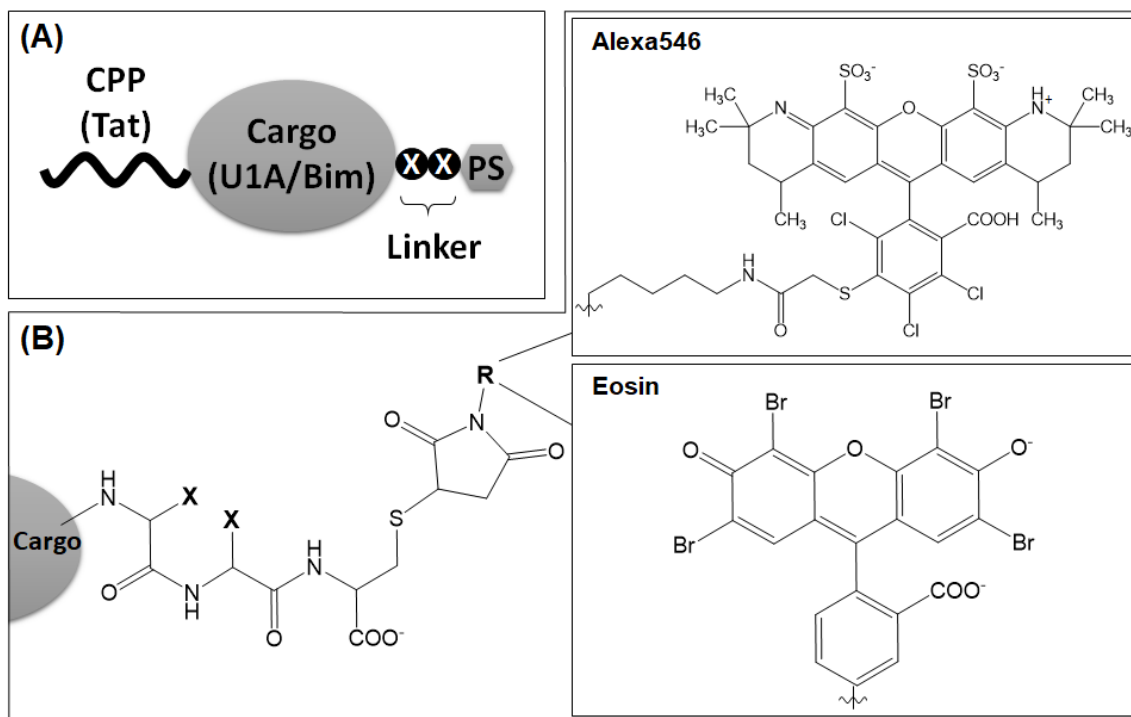


Figure 2-1. Structures of CPP-cargo-linker-PS. (A) Diagram of CPP-cargo-linker-PS.

(B) Chemical structures of the linker-PS moiety. R shows the photosensitizer. X shows the X amino acid side chain.

Materials and Methods

Preparation of TatBim-XX-Alexa546 and TatBim-XX-eosin

TatBim-XX-C peptides (X = A, D, E, F, G, H, K, L, N, R, S, V, or W) (Table 2-1) were prepared by conventional Fmoc-based solid-phase peptide synthesis. These peptides contained a cysteine at the C-terminus for reaction with a maleimide group of photosensitizers, Alexa Fluor 546 C5 maleimide (Life Technologies, Carlsbad, CA, USA) and eosin-5-maleimide (Invitrogen, Waltham, MA, USA). The TatBim-XX-C peptide was reacted with each dye to generate TatBim-XX-Alexa546 or TatBim-XX-eosin (Scheme 2-1). These peptide-photosensitizer conjugates were purified by a reversed-phase HPLC (Symphonia C18 Column [4.6 × 150 mm, 5 μm particle diameter; Jasco, Tokyo, Japan]) eluted with 0.1% aqueous trifluoroacetic acid (A)/acetonitrile (B) gradient mixture (B: 0 min; 0%, 10 min; 40%, 30 min; 65%, 40 min; 100%) at a flow rate of 0.6 mL/min. The purified TatBim-XX-PS conjugates were analyzed by sodium dodecyl sulfate-polyacrylamide gel electrophoresis (SDS-PAGE). Photosensitizer-attachment efficiencies to the TatBim-XX-C peptide were calculated by measuring absorbance at the peptide and photosensitizer peak wavelengths. Photosensitizer attachment efficiencies were adjusted to 50% for TatBim-XX-Alexa546 and 20% for TatBim-XX-eosin using separately prepared unmodified TatBim-XX peptides.

Preparation of TatU1A-XX-Alexa546

The RNA carrier protein TatU1A-XX, bearing a C-terminal Cys residue, was prepared as described previously^{5, 34}. The purified recombinant TatU1A-XX protein (20–30 μ M) and Alexa Fluor 546 C5 maleimide (25 μ M) were mixed in a buffer containing 50 mM HEPES-KOH (pH 7.6), 100 mM $(\text{NH}_4)_2\text{SO}_4$, 200 mM imidazole, and 20% glycerol and incubated at 25 °C for 1 h. The Alexa546-modified TatU1A-XX molecules (TatU1A-XX-Alexa546) were purified using a Centri-Sep Spin Column (Princeton Separations, Freehold, NJ, USA) equilibrated with T buffer [20 mM HEPES-KOH (pH 7.6), 115 mM NaCl, 5.4 mM KCl, 1.8 mM CaCl_2 , 0.8 mM MgCl_2 , and 13.8 mM glucose]. The purified TatU1A-XX-Alexa546 was analyzed by SDS-PAGE. The protein concentration was determined using a Protein Assay Kit (Bio-Rad Laboratories, Hercules, CA, USA). Photosensitizer-attachment efficiencies to the carrier proteins were adjusted to 20% using separately prepared unlabeled carrier proteins.

Cellular internalization of TatBim-XX-PS and TatU1A-XX-Alexa546/shRNA

CHO cells were cultured in Ham's F-12 medium (Nacalai Tesque, Kyoto, Japan), supplemented with 10% fetal bovine serum (FBS; Sigma-Aldrich, St. Louis, MO, USA), 100 U/mL penicillin, and 100 μ g/mL streptomycin (Gibco, Carlsbad, CA, USA). CHO cells were grown in 96-well plates to 70% confluence, washed twice with T buffer, and treated with TatBim-XX-PS or TatU1A-XX-Alexa546/shRNA.

For TatBim-XX-PS, the cells were treated for 3 h with TatBim-XX-Alexa546 (2 μ M) and TatBim-XX-eosin (4 μ M). For the TatU1A-XX-Alexa546/shRNA complex, non-specific shRNA (120 nM, 5'- GAU UAU GUC CGG UUA UGU ACA UUG CAC UCC GUA CAU AAC CGG ACA UAA UC dT-Fam-3', purchased from JBioS (Saitama, Japan)) and TatU1A-Alexa546 (1.2 μ M) were mixed in T buffer and incubated at 37 °C for 10 min. The cells in 96-well plates were treated for 2 h with the TatU1A-XX-Alexa546/shRNA complex.

After washing twice with T buffer, the cells were irradiated using a mercury lamp (Olympus USH-1030L; Tokyo, Japan) passed through a 12% ND filter, a U-MWIG3 mirror unit (530-550 nm), and a 40 \times objective lens on a IX51 fluorescence microscope (Olympus). The light dose was 10 J/cm². At 2-3 min after irradiation, fluorescence images were acquired using the IX51 fluorescence microscope. The photoinduced endosomal escape efficiencies of TatBim-XX-PS and TatU1A-XX-Alexa546 were calculated by counting the number of cells in which fluorescence was dispersed within the cytosol after photostimulation (NF) and the total cell number (NT) using fluorescence and phase-contrast images from the same area. The endosomal escape efficiency (%) was defined as $NF/NT \times 100$.

Observation of photoinduced apoptosis

CHO cells were treated with 2 μ M TatBim-XX-Alexa546 for 3 h at 37 °C and then

irradiated as described above. The cells were further incubated for 5 h at 37 °C. The apoptotic cells were stained for 30 min at 37 °C using the NucView 488 Caspase-3 Assay Kit (Biotium, Fremont, CA, USA), a marker of early apoptosis. Fluorescence images were captured using the IX51 fluorescence microscope. Cells incubated at 37 °C for 5 h with medium containing 1 μ M staurosporine were used as a positive control.

Measurement of the $^1\text{O}_2$ quantum yields of XX-eosin

XX-eosin (X = E, F, K, L, and W) (Table 1) were prepared as described in the above section “Preparation of TatBim-XX-Alexa546 and TatBim-XX-eosin.” and analyzed by electrophoresis. The $^1\text{O}_2$ quantum yields of XX-eosin molecules were calculated by comparing the emission intensities of the singlet oxygen photosensitized by each dye at 1270 nm using eosin Y as the standard. The $^1\text{O}_2$ quantum yields of XX-eosin (0.9 μ M) were measured in the D_2O solution including 100 mM NaOAc (pH 5.5) and 0.25% dimethyl sulfoxide. In detail, a nanosecond-pulsed Nd:YAG laser pumped dye (C500 in MeOH) laser (500 Hz, pulse width 7 ns, 10 mW) was used as the excitation source, and the emission from a singlet oxygen from the dye was collected by the bundle fiber and detected by the near infrared-photomultiplier tube (NIR-PMT) (H10330B-45: Hamamatsu Photonics K.K., Hamamatsu, Japan) through the band-pass filter (1270 nm) and recorded by the multi-channel scaler (Nano-Harp 250; Pico-Quant, Berlin, Germany) for 60 s. The decay curves at 1270 nm ($^1\text{O}_2$ emission) were obtained. The lifetime of

photogenerated $^1\text{O}_2$ was calculated using FluoFit global fluorescence decay data analysis software (PicoQuant GmbH, Berlin, Germany). The emission signal intensity was calculated by accumulating the intensity of the decay curve from 200 ns to 300 μs . The $^1\text{O}_2$ quantum yields (ϕ_Δ) of each dye in the D_2O solution were calculated by comparing the intensity of the signal of each dye to that of eosin Y in the D_2O solution.

Results

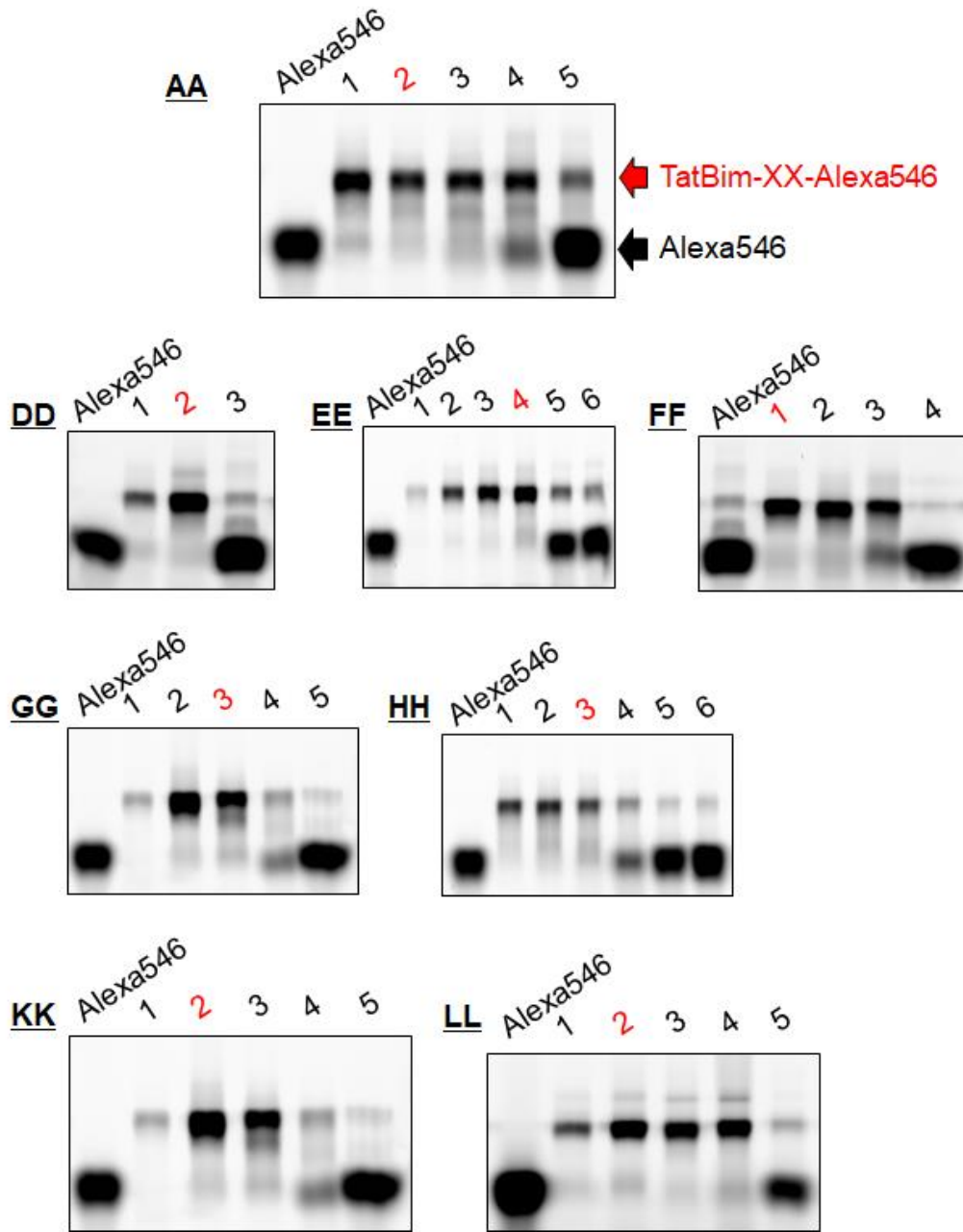
Photoinduced endosomal escape and apoptosis efficiency of TatBim-XX-Alexa546

To investigate the influence of linker amino acids (XX) on PCI efficiency, we prepared TatBim-XX-Alexa546 molecules (Table 2-1). The yields of TatBim-XX-Alexa546 molecules were 12-25% after the reaction (Scheme 2-1) and HPLC purification (Fig. 2-2). Chinese hamster ovary (CHO) cells were treated with the conjugates and visualized by fluorescence microscopy. All TatBim-XX-Alexa546 molecules showed patchy localization before irradiation (Fig. 2-3A), indicating that these molecules were entrapped in endosomes. After irradiation (10 J/cm^2), the cytosolic dispersion of TatBim-XX-Alexa546 was observed with significantly different efficiencies depending on the linker XX sequence (Fig. 2-3). TatBim-FF-Alexa546 and TatBim-LL-Alexa546 showed the highest endosomal escape efficiencies (PCI efficiencies) of around 70%, followed by 59% for the AA conjugate and 35% for the VV conjugate. (Fig. 2-3B). Endosomal escape efficiencies of TatBim-XX-Alexa546 were highly related to the rate of apoptosis (Fig. 2-3C). TatBim-XX-Alexa546 with an endosomal escape efficiency of less than 20% induced minimal apoptosis. TatBim-XX-Alexa546 molecules with a hydrophobic linker, except for WW, tended to show higher endosomal escape/apoptosis efficiencies than those of molecules with a hydrophilic linker.

Table 2-1. Sequences of peptide/protein-photosensitizer (PS) conjugates

Peptide-PS conjugates	Sequence (from N to C terminus)
TatBim-XX-PS	RKKRRQRRR-EIWIAQELRRIGDEFNAYYAR-XX- C-PS (X = A, D, E, F, G, H, K, L, N, R, S, V, or W) (PS = Alexa546 or eosin)
TatU1A-XX-Alexa546 (C terminal 30 aa)	-MQGFPPFYDKPMRIQYAKTDSDIKMK-XX-C- Alexa546 (X = E, F, K, L, S, or W)
EE-eosin	WG-EE-C-eosin
FF-eosin	WG-FF-C-eosin
KK-eosin	WG-KK-C-eosin
LL-eosin	WG-LL-C-eosin
WW-eosin	WG-WW-C-eosin

TatBim-XX-PS and TatU1A-XX-Alexa546 are examples of CPP-cargo-XX-PS, in which XX means linker amino acids. Tat peptide was used as a CPP. Bim peptide and U1A protein were used as cargoes.



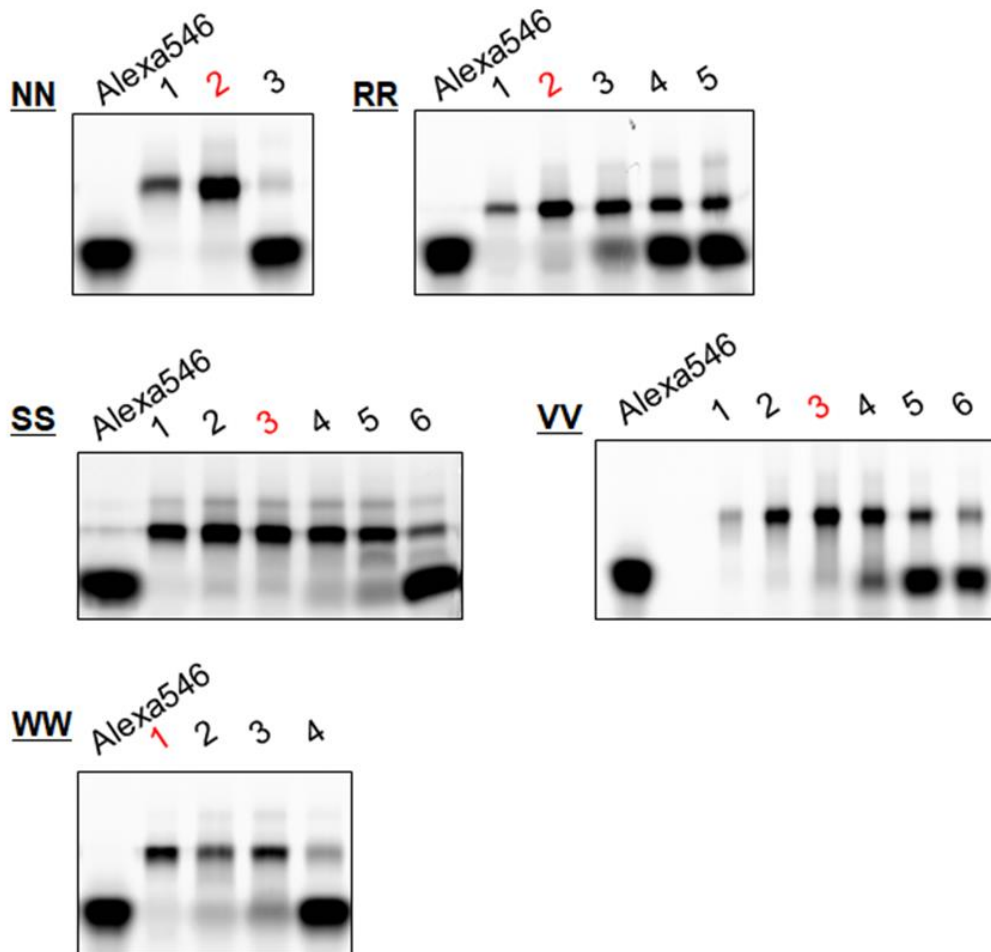


Figure 2-2. Analysis of TatBim-XX-Alexa546 molecules by 18% SDS-PAGE. The reaction mixture including TatBim-XX-C and Alexa Fluor 546 C5 maleimide was loaded on the reverse-phase HPLC, the HPLC peak fractions were analyzed. Red peak number indicates a fraction which we used as TatBim-XX-Alexa546 for the cell treatment. Alexa546 images of the gels were acquired using an FLA-9000 (Fujifilm, Japan).

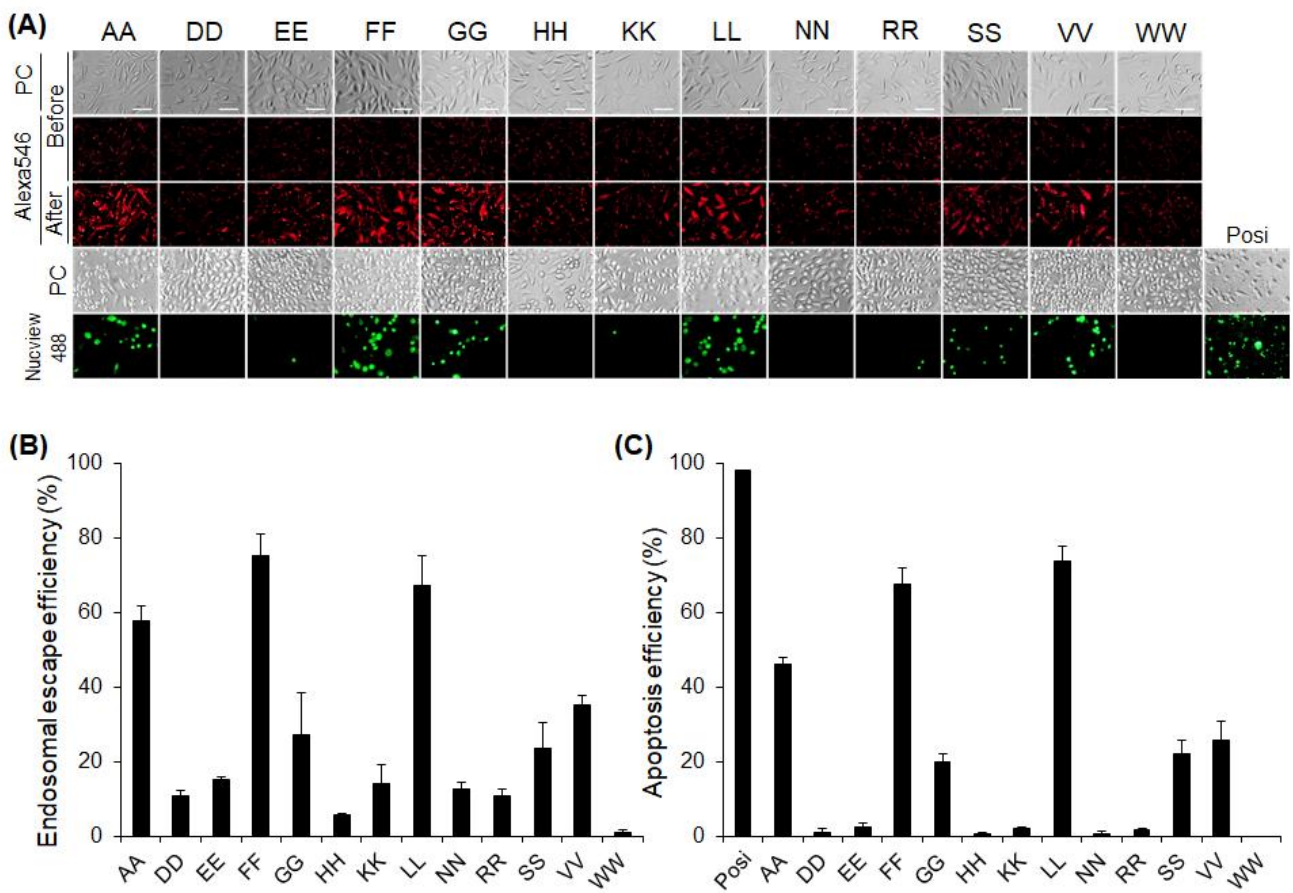


Figure 2-3. Internalization of TatBim-XX-Alexa546 by CHO cells. (A) Cells were treated with TatBin-XX-Alexa546 and irradiated. In the upper three rows, phase contrast (PC) and Alexa546 images of the cells before and after 10 J/cm² irradiation are shown. In the lower rows, phase contrast and NucView488 images of cells after irradiation followed by 5 h of incubation and NucView 488 staining are shown. Staurosporine (1.0 μM) was used as a positive control (Posi). Scale bars indicate 50 μm. (B) Photoinduced escape efficiencies of TatBim-XX-Alexa546. (C) Apoptosis efficiencies of TatBim-XX-Alexa546. Data shown in (B) and (C) are means ± SEM of three independent experiments.

Photoinduced endosomal escape of TatBim-XX-eosin

TatBim-XX-eosin molecules were synthesized by the reaction shown in Fig. 2-1. The yields of TatBim-XX-eosin molecules were 10-22% after the reaction and HPLC purification. We analyzed the endosomal escape efficiency of TatBim-XX carrying eosin, instead of Alexa546, to determine whether the optimal linker for efficient endosomal escape depends on the photosensitizer. For subsequent analyses, we selected six representative linkers, including hydrophobic (LL, FF, WW), hydrophilic (SS), anionic (EE), and cationic (KK) linkers. As shown in Fig. 2-4, endosomal escape efficiencies of TatBim-FF-eosin and TatBim-LL-eosin were higher than those of other conjugates, consistent with the results obtained using TatBim-XX-Alexa546.

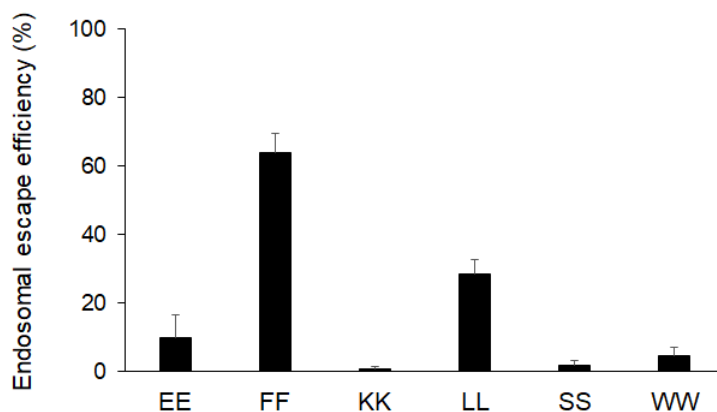


Figure 2-4. Internalization of TatBim-XX-eosin by CHO cells. Photoinduced endosomal escape efficiencies of TatBim-XX-eosin are shown. Data are means \pm SEM of three independent experiments.

Photoinduced endosomal escape of TatU1A-XX-Alexa546

We prepared TatU1A-XX-Alexa546/shRNA complexes (Fig. 2-5) to further investigate the effect of the linker sequence on photoinduced endosomal escape. The yields of TatU1A-XX-Alexa546 molecules were 15-25% after the reaction (Scheme 2-1) and purification. The TatU1A-XX-Alexa546/shRNA complex is also a Tat-cargo-photosensitizer complex but carries U1A/shRNA instead of Bim as cargo (used in the above-described analyses). As shown in Fig. 2-3, 2-4, 2-6, TatU1A-EE-Alexa546 and TatU1A-LL-Alexa546 showed the highest endosomal escape efficiencies of around 80%, followed by TatU1A-FF-Alexa546 (~50%). The increases in endosomal escape for LL and FF linkers were consistent with the results for TatBim-XX-PS.

The analysis of the cellular internalization of CPP-cargo-XX-PS conjugates revealed that the conjugates with FF or LL linkers were highly efficient in endosomal escape (Fig. 2-3, 2-4, 2-6). This superiority of FF and LL linkers was commonly observed even with different cargoes (Bim vs. U1A) or photosensitizers (Alexa546 vs. eosin).

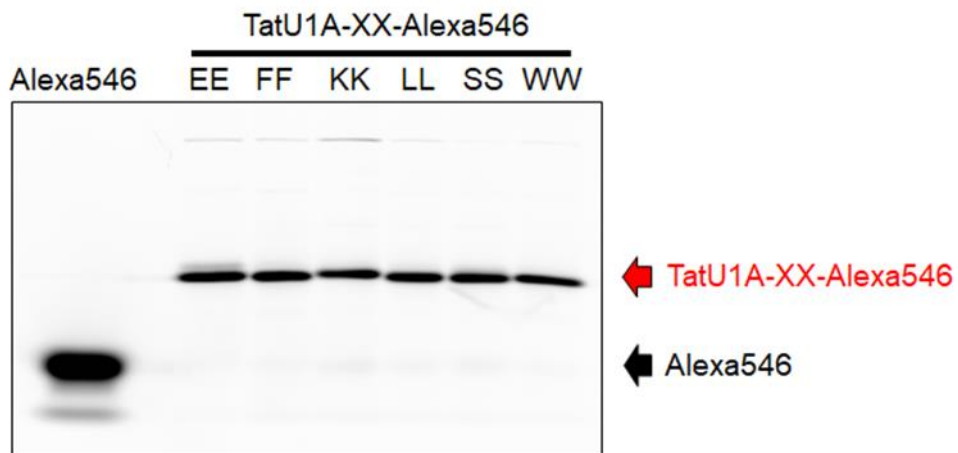


Figure 2-5. Analysis of TatU1A-XX-Alexa546 conjugates by 18% SDS-PAGE. Each conjugate was analyzed after purification of the conjugate using a Centri-Sep Spin Column. Alexa546 images of the gels were acquired using an FLA-9000 (Fujifilm).

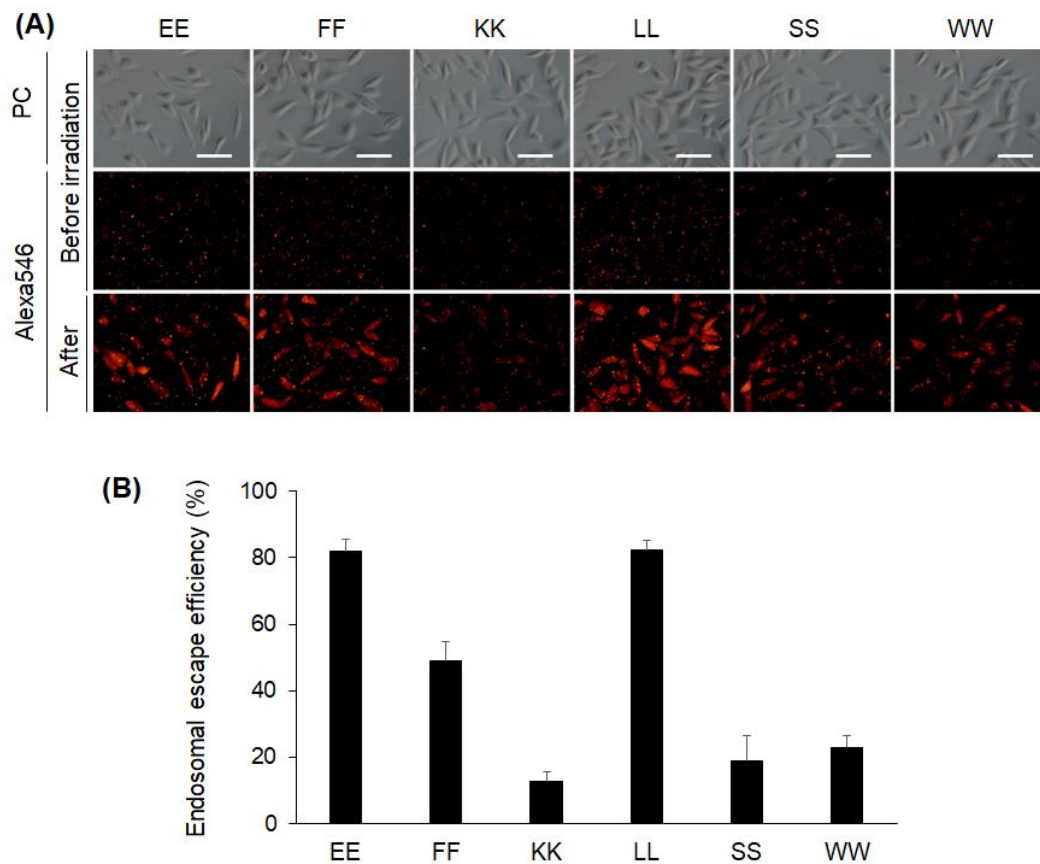


Figure 2-6. Internalization of TatU1A-XX-Alexa546 by CHO cells. (A) Cells were treated with TatU1A-XX-Alexa546 and shRNA and irradiated. Images of cells before and after 10 J/cm² irradiation are shown. Scale bars indicate 50 μ m. (B) Photoinduced endosomal escape efficiencies of TatU1A-XX-Alexa546. Data are means \pm SEM of three independent experiments.

Effect of linker amino acids on $^1\text{O}_2$ quantum yields

PCI is generally believed to be mediated by $^1\text{O}_2$ photogenerated from photosensitizers in endosomes⁷⁻⁹. Our previous work has also shown that photogenerated $^1\text{O}_2$ mediates the endosomal escape of the TatU1A-PS/RNA complex¹⁰. Thus, we next investigated the contribution of the adjacent XX linker toward the $^1\text{O}_2$ quantum yield of a photosensitizer. For this experiment, eosin was used as a photosensitizer owing to its relatively high $^1\text{O}_2$ quantum yield (0.58 in D_2O)²⁹ and the ease of measuring $^1\text{O}_2$ generation from eosin. Since it is difficult to prepare the pure, large quantities of long peptides (TatU1A-XX-eosin or TatBim-XX-eosin) needed for $^1\text{O}_2$ measurement, eosin-bound short peptides (XX-eosin) (Table 2-1) were used for the measurement of photogenerated $^1\text{O}_2$. Absorption and fluorescence excitation spectra indicated that XX-eosin dimers or multimers were almost undetectable (Fig. 2-7, 2-8). As shown in Table 2-2, the $^1\text{O}_2$ quantum yields (ϕ_Δ) of XX-eosin molecules ranged from 0.10 to 0.36. LL- and FF-eosin had 2.4–3.6 times higher $^1\text{O}_2$ quantum yields than KK- or WW-eosin. All peptide-modified eosin molecules and even the maleimide-modified eosin had much lower ϕ_Δ values than that of non-modified eosin, indicating that the modifications greatly affected the $^1\text{O}_2$ photogeneration efficiency of eosin.

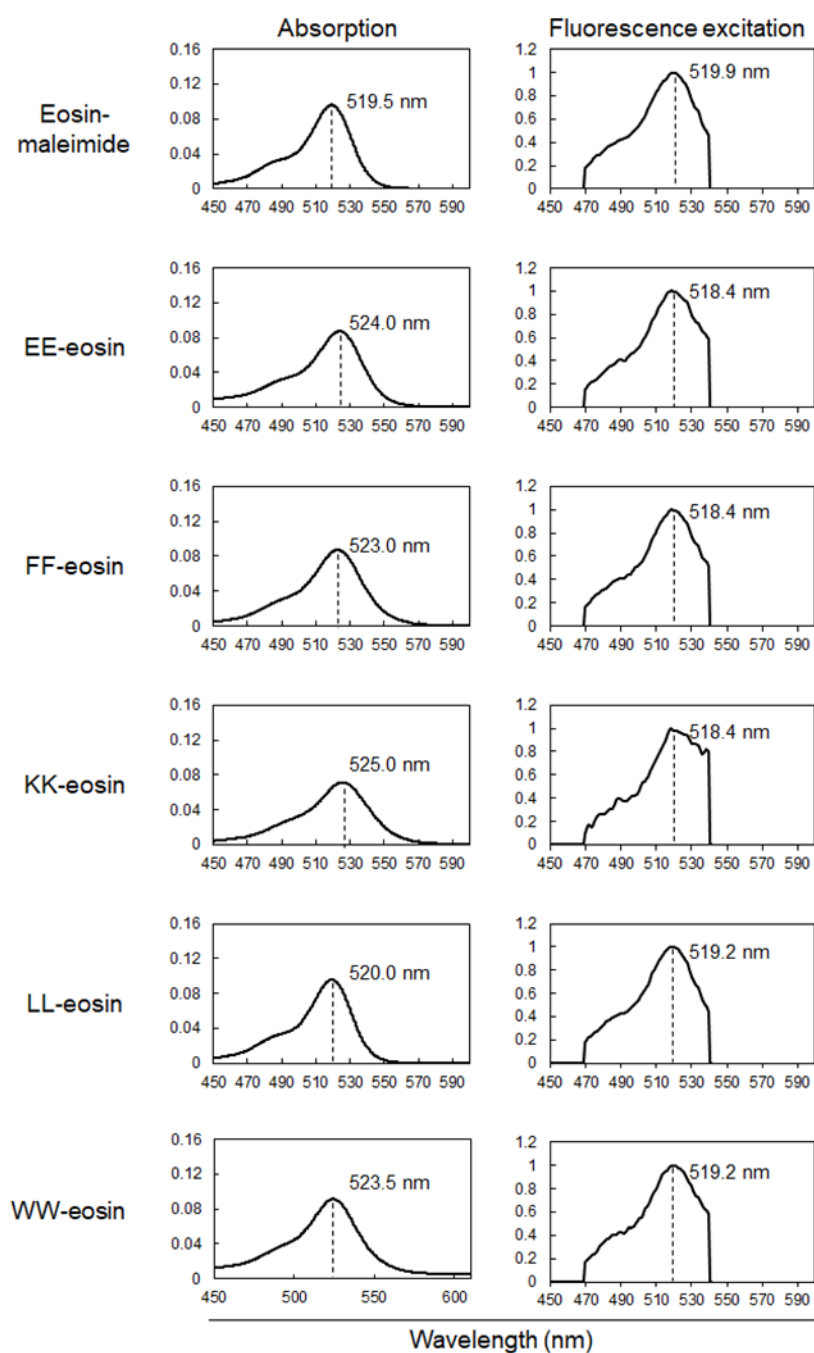


Figure 2-7. Absorption (left) and fluorescence excitation (right) spectra of eosin-maleimide and XX-eosin molecules. The number in each spectrum indicates the peak wavelength. Absorption and fluorescence excitation spectra of the eosin derivatives (1 μM) were measured in the D_2O solution including 100 mM NaOAc (pH 5.5) and 0.25%

dimethyl sulfoxide. Fluorescence excitation spectra (470-540 nm) were measured at emission wavelength from 550 nm to 680 nm using Absolute PL quantum yield spectrometer (C9920-02, Hamamatsu Photonics K.K., Hamamatsu, Japan).

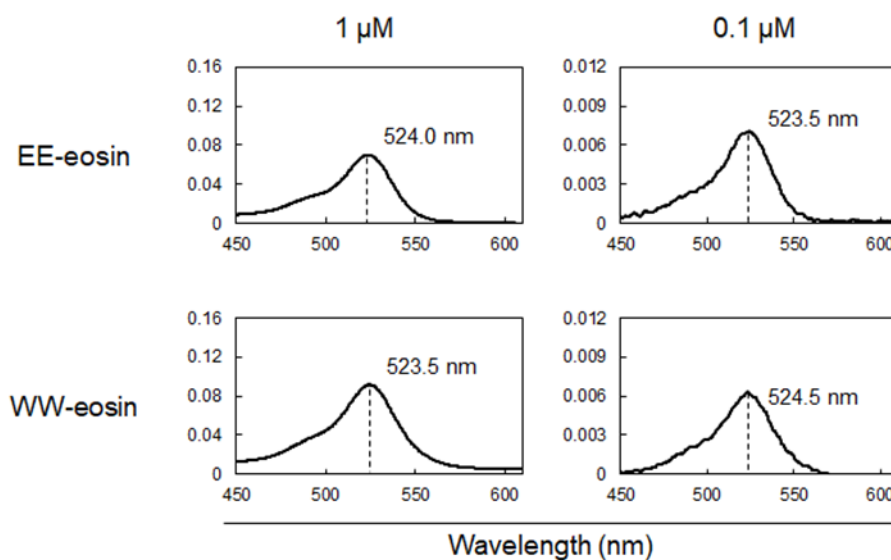


Figure 2-8. Absorption spectra of EE-eosin and WW-eosin at different concentrations (1 μM and 0.1 μM). The number in each spectrum indicates the peak wavelength. The absorption spectra were measured using an U-3500 spectrophotometer (Hitachi, Japan).

Table 2-2. Singlet oxygen quantum yields (ϕ_{Δ}) of eosin derivatives

Eosin derivatives	ϕ_{Δ}
Eosin	0.58
Eosin-5-maleimide	0.26
EE-eosin	0.14
FF-eosin	0.26
KK-eosin	0.11
LL-eosin	0.36
WW-eosin	0.10

Discussion

Previously, we developed CPP-cargo-PS conjugates, such as TatBim-PS and TatU1A-PS, to photoinduce apoptosis and intracellular RNA delivery, respectively. This strategy can be used for the photoinduction of any target function in cells by preparing a new CPP-cargo-PS conjugate in which the cargo protein/peptide has the appropriate function. However, many conjugates do not result in sufficient photoinduction of the function. We hypothesized that the amino acid sequence adjacent to the photosensitizer is a major determinant of the PCI efficiency of CPP-cargo-PS conjugates. Although we cannot change the C-terminal sequence of a cargo molecule, we can add an amino acid linker sequence between the cargo C-terminus and photosensitizer in newly designed CPP-cargo-PS conjugates.

In this study, to improve the success rate of developing CPP-cargo-PS conjugates, we investigated the effect of the linker between the cargo and photosensitizer on PCI. In particular, we prepared three types of CPP-cargo-PS conjugates: TatBim-XX-Alexa546, TatBim-XX-eosin, and TatU1A-Alexa546. Using TatBim-XX-Alexa546, the conjugates with hydrophobic linkers (FF, LL, AA, and VV but not WW) showed higher endosomal escape efficiencies than those of conjugates with hydrophilic linkers (Fig. 2-3). The FF and LL linkers were optimal for PCI of TatBim-XX-Alexa546 and apoptosis induction. The FF and LL linkers were also optimal for TatBim-XX-eosin and TatU1A-XX-Alexa546 (Fig. 2-4, 2-6) with respect to escape from endosomes. Accordingly, the FF or

LL linker should be the first choice in future designs of CPP-cargo-PS conjugates.

In contrast to broad effectiveness of the FF and LL linkers, the EE linker only efficiently enhanced PCI in the TatU1A-XX-Alexa546 platform (Fig. 2-6). This result indicates that linker performance is partially affected by the cargo moiety. Additionally, the linker preference differed slightly between TatBim-XX-Alexa546 and TatBim-XX-eosin (Fig. 2-3, 2-4), indicating that it is partially affected by the photosensitizer moiety. It is not clear why the EE linker enhanced PCI only in the TatU1A-XX-Alexa546 platform. It is possible that the C-terminal cationic amino acids of the cargo (the C-terminal 3 amino acids include two Lys in U1A and one Arg in Bim) affect the characteristics of the anionic EE linker.

The singlet oxygen quantum yields of XX-eosin molecules could partially explain the difference in PCI efficiency among the linkers. The higher $^1\text{O}_2$ quantum yields of LL- and FF-eosin (Table 2-2) may be related to the increase in PCI efficiency by the LL and FF linkers (Fig. 2-4). Low PCI efficiencies with the KK and WW linkers can likely be explained, in part, by the low $^1\text{O}_2$ quantum yields of KK- and WW-eosin. However, although the $^1\text{O}_2$ quantum yields of LL- and FF-eosin are 2.4–3.6 times higher than KK- or WW-eosin, this difference could only partially explain the 6–85 times higher PCI efficiencies obtained with the LL and FF linkers relative to those obtained with the KK and WW linkers.

The difference in PCI efficiencies might be related to differences in interactions

between each XX linker-PS moiety and the endosomal membrane. The lifetime of $^1\text{O}_2$ is much longer in the lipid membrane than in water ³¹. Thus, the localization of the photosensitizer in the endosomal membrane is considered to be important for PCI efficiency. Ehrenberg et al. have demonstrated the relationships between the depths of porphyrin derivative insertions in lipid membranes and the photosensitizing efficiencies of the porphyrin derivatives and found that photosensitizers incorporated deeper into the membranes are more efficient ^{32, 33}. MacRobert et al. have reported the photoproperties of CPP-chlorin e₆ conjugates and commented that the insertion of a hydrophobic spacer unit between the photosensitizer and peptide moieties potentially enables the deeper penetration of the photosensitizer into the membrane lipid bilayer, thereby causing a more effective oxidative damage to the membrane ³⁰. Thus, the hydrophobicities of the XX linkers in the CPP-cargo-XX-PS conjugates potentially affect the interactions between the PS and endosomal membrane. The hydrophobic LL and FF linkers may bring PS closer to the hydrophobic core of the lipid bilayer and enhance the photo-dependent destabilization of the endosomal membrane.

Our results demonstrated that the PCI efficiencies of CPP-cargo-PS conjugates are largely determined by the linker amino acids between the cargo and photosensitizer. In particular, hydrophobic FF and LL linkers enhanced the photoinduced endosomal escape of conjugates. Future studies are needed to determine the factors contributing to the effects of the FF and LL linkers as well as the mechanism underlying the interaction

between these linker-PS moieties and the endosomal membrane. This study provides a basis for the design of CPP-cargo-PS conjugates for protein/peptide-based PCI and photodynamic therapy. The FF or LL linker should be used in future CPP-cargo-PS conjugates, and some other linkers, such as KK and WW, should not be used owing to their negative effects on $^1\text{O}_2$ generation from photosensitizers. To further optimize the linker, sequences other than XX (2-aa repeat) should be examined in future. Despite the large number of candidates (>8000, even if no more than 3-aa sequences are considered), our results suggest that the candidates could be narrowed down by using sequences containing L or F.

References

- (1) Fawell S, Seery J, Daikh Y, Moore C, Chen LL, Pepinsky B, Barsoum J. (1994) Tat-mediated delivery of heterologous proteins into cells. *Proc Natl Acad Sci USA*. 91, 664–668.
- (2) Futaki S, Hirose H, Nakase I. (2013) Arginine-rich peptides: methods of translocation through biological membranes. *Curr Pharm Des*. 19, 2863–2868.
- (3) Kristensen M, Birch D, Nielsen HM. (2016) Applications and challenges for use of cell-penetrating peptides as delivery vectors for peptide and protein cargos. *Int J Mol Sci*. 17, 185.
- (4) Fu A, Tang R, Hardie J, Farkas ME, Rotello VM. (2014) Promises and pitfalls of intracellular delivery of proteins. *Bioconjug Chem*. 25, 1602–1608.
- (5) Endoh T, Sisido M, Ohtsuki T. (2008) Cellular siRNA delivery mediated by a cell-permeant RNA-binding protein and photoinduced RNA interference. *Bioconjug Chem*. 19, 1017–1024.
- (6) Watanabe K, Fujiwara H, Kitamatsu M, Ohtsuki T. (2016) Photoinduced apoptosis using a peptide carrying a photosensitizer. *Bioorg Med Chem Lett*. 26, 3115–3118.
- (7) Berg K, Selbo PK, Prasmickaite L, Tjelle TE, Sandvig K, Moan J, Gaudernack G, Fodstad Ø, Kjølrsrud S, Anholt H, Rodal GH, Rodal SK, Høgset A. (1999) Photochemical internalization: a novel technology for delivery of

macromolecules into cytosol. *Cancer Res.* 59, 1180–1183.

- (8) Oliveira S, Fretz MM, Høgset A, Storm G, Schiffelers RM. (2007) Photochemical internalization enhances silencing of epidermal growth factor receptor through improved endosomal escape of siRNA. *Biochim Biophys Acta.* 1768, 1211–1217.
- (9) Haug M, Brede G, Håkerud M, Nedberg AG, Gederaas OA, Flo TH, Edwards VT, Selbo PK, Høgset A, Halaas Ø. (2018) Photochemical internalization of peptide antigens provides a novel strategy to realize therapeutic cancer vaccination. *Front Immunol.* 9, 1–14.
- (10) Meerovich I, Muthukrishnan N, Johnson GA, Erazo-Oliveras A, Pellois JP. (2014) Photodamage of lipid bilayers by irradiation of a fluorescently labeled cell-penetrating peptide. *Biochim Biophys Acta.* 1840, 507-515.
- (11) Ohtsuki T, Miki S, Kobayashi S, Haraguchi T, Nakata E, Hirakawa K, Sumita K, Watanabe K, Okazaki S. (2015) The molecular mechanism of photochemical internalization of cell penetrating peptide-cargo-photosensitizer conjugates. *Sci Rep.* 5, 18577.
- (12) Wang TY, Libardo MDJ, Angeles-Boza AM, Pellois JP. (2017) Membrane oxidation in cell delivery and cell killing applications. *ACS Chem Biol.* 12, 1170.
- (13) Yarani R, Shiraishi T, Nielsen PE. (2018) Effective photo-enhancement of cellular activity of fluorophore-octaarginine antisense PNA conjugates correlates

with singlet oxygen formation, endosomal escape and chromophore lipophilicity.

Sci Rep. 8, 12–15.

- (14) Wang JT, Giuntini F, Eggleston IM, Bown SG, MacRobert AJ. (2012) Photochemical internalisation of a macromolecular protein toxin using a cell penetrating peptide-photosensitiser conjugate. *J Control Release.* 157, 305–313.
- (15) Muthukrishnan N, Donovan S, Pellois JP. (2014) The photolytic activity of poly-arginine cell penetrating peptides conjugated to carboxy-tetramethylrhodamine is modulated by arginine residue content and fluorophore conjugation site. *Photochem Photobiol.* 90, 1034–1042.
- (16) Dondi R, Yaghini E, Tewari KM, Wang L, Giuntini F, Loizidou M, MacRobert AJ, Eggleston IM. (2016) Flexible synthesis of cationic peptide-porphyrin derivatives for light-triggered drug delivery and photodynamic therapy. *Org Biomol Chem.* 14, 11488–11501.
- (17) Yaghini E, Dondi R, Edler KJ, Loizidou M, MacRobert AJ, Eggleston IM. (2018) Codelivery of a cytotoxin and photosensitiser via a liposomal nanocarrier: a novel strategy for light-triggered cytosolic release. *Nanoscale.* 10, 20366–20376.
- (18) Matsushita-Ishiodori Y, Kuwabara R, Sakakoshi H, Endoh T, Ohtsuki T. (2011) Photosensitizing carrier proteins for photoinducible RNA interference. *Bioconjug Chem.* 22, 2222–2226.
- (19) Matsushita-Ishiodori Y, Morinaga M, Watanabe K, Ohtsuki T. (2013) Near-

- infrared light-directed RNAi using a photosensitive carrier molecule. *Bioconjug Chem.* 24, 1669–1673.
- (20) Shiraga K, Soe TH, Matsumoto S, Watanabe K, Ohtsuki T. (2018) Red and near-infrared light-directed cytosolic delivery of two different RNAs using photosensitive RNA carriers. *Bioconjug Chem.* 29, 3174–3179.
- (21) Endoh T, Shintani R, Mie M, Kobatake E, Ohtsuki T, Sisido M. (2009) Detection of bioactive small molecules by fluorescent resonance energy transfer (FRET) in RNA-protein conjugates. *Bioconjug Chem.* 20, 2242–2246.
- (22) Mojziso娃 H, Bonneau S, Maillard P, Berg K, Brault D. (2009) Photosensitizing properties of chlorins in solution and in membrane-mimicking systems. *Photochem Photobiol Sci.* 8, 778–787.
- (23) Jinadasa RG, Zhou Z, Vicente MG, Smith KM. (2016) Syntheses and cellular investigations of di-aspartate and aspartate-lysine chlorin e6 conjugates. *Org Biomol Chem.* 14, 1049-1064.
- (24) Bronshtein I, Afri M, Weitman H, Frimer AA, Smith KM, Ehrenberg B. (2004) Porphyrin depth in lipid bilayers as determined by iodide and parallax fluorescence quenching methods and its effect on photosensitizing efficiency. *Biophys J.* 87, 1155–1164.
- (25) Estevão BM, Pellosi DS, Freitas CF, Vanzin D, Santana D. (2014) Interaction of eosin and its ester derivatives with aqueous biomimetic micelles: evaluation of

- photodynamic potentialities. *J Photochem Photobiol A Chem.* 287, 30-39.
- (26) Liu G, Hu J, Zhang G, Liu S. (2015) Rationally engineering phototherapy modules of eosin-conjugated responsive polymeric nanocarriers via intracellular endocytic pH gradients. *Bioconjug Chem.* 26, 1328-1338.
- (27) Dobos A, Steiger W, Theiner D, Gruber P, Lunzer M, Hoorick JV, Vlierberghe SV, Ovsianikov A. (2019) Screening of two-photon activated photodynamic therapy sensitizers using a 3D osteosarcoma model. *Analyst.* 144, 3056-3063.
- (28) Endoh T, Sisido M, Ohtsuki T. (2009) Spatial regulation of specific gene expression through photoactivation of RNAi. *J Control Release.* 137, 241-245.
- (29) Redmond RW, Gamlin JN. (1999) A compilation of singlet oxygen yields from biologically relevant molecules. *Photochem Photobiol.* 70, 391-475.
- (30) Yaghini, E, Dondi R, Tewari MK, Loizidou M, Eggleston MI, MacRobert JA. (2017) Endolysosomal targeting of a clinical chlorin photosensitizer for light-triggered delivery of nano-sized medicines. *Sci Rep* 7, 6059.
- (31) Ehrenberg B, Anderson JL, Foote CS. (1998) Kinetics and yield of singlet oxygen photosensitized by hypericin in organic and biological media. *Photochem Photobiol.* 68, 135-140.
- (32) Lavi A, Weitman H, Holmes RT, Smith KM, Ehrenberg B. (2002) The depth of porphyrin in a membrane and the membrane's physical properties affect the

photosensitizing efficiency. *Biophys J.* 82, 2101– 2110.

- (33) Bronshtein I, Afri M, Weitman H, Frimer AA, Smith KM, Ehrenberg B. (2004) Porphyrin Depth in Lipid Bilayers as Determined by Iodide and Parallax Fluorescence Quenching Methods and Its Effect on Photosensitizing Efficiency. *Biophys J.* 87, 1155–1164.
- (34) Endoh T, Ohtsuki T. (2010) Cellular siRNA delivery using TatU1A and photo-induced RNA interference. *Methods Mol Biol.* 623, 271-281.

List of publications

- [1] J. Li., C. Xu., N. Shimada., Y. Miyoshi., K. Watanabe., W. Cong., T. Ohtsuki.
Detection of small, highly structured RNAs using molecular beacons. *Analytical Methods*, 20, 2971-2976 (2017).
- [2] Y. Miyoshi., T. Ohtsuki., H. Kashida., H. Asanuma., K. Watanabe. In-stem molecular beacon targeted to a 5'-region of tRNA inclusive of the D arm that detects mature tRNA with high sensitivity. *PLOS ONE*, 14, e0211505 (2019).
- [3] Y. Miyoshi., K. Watanabe. Formation mechanism and cellular functions of nuclear stress bodies induced by heat stress. *Thermal Medicine*, 34 (3), 23-34 (2018).
- [4] Y. Miyoshi., M. Kadono., S. Okazaki., A. Nishimura., M. Kitamatsu., K. Watanabe., T. Ohtsuki. Endosomal escape of peptide-photosensitizer conjugates is affected by amino acid sequences near the photosensitizer. *Bioconjug Chem*, submitted (2020).

Acknowledgment

I wish to express my sincere gratitude to Professor Takashi Ohstuki for his kind permission to perform this study under his supervision in Biomolecular Engineering Laboratory during 2014-2020. I wish to express my sincere thanks for his kindness, patience and encouragement throughout this study.

I would like to thank the thesis reviewing committee and co-supervisors, Professor Hiroshi Tokumitsu and Associate Professor Ayano Sato, for their valuable comments and insightful suggestions for my thesis.

I wish to express my sincere gratitude to Assistant Professor Dr. Kazunori Watanabe for his valuable suggestions and the detailed discussions for each experiment in this study. I am also thankful for his kind support and all the help during my study.

I am deeply grateful to Associate Professor at Kinki university Dr. Mizuki Kitamatsu for his support in synthesizing a series of peptides.

I greatly appreciate all members and graduates of the Professor Ohtsuki's laboratory for their kindness and warm hospitality. In particular, I am thankful to Technical Staff, Yukiko Kurimoto for her great supports .

I gratefully acknowledge the Suga Hiroaki scholarship received from Okayama University.

Yuichi Miyoshi